Disclaimer

This note has not been internally reviewed by the DØ Collaboration. Results or plots contained in this note were only intended for internal documentation by the authors of the note and they are not approved as scientific results by either the authors or the DØ Collaboration. All approved scientific results of the DØ Collaboration have been published as internally reviewed Conference Notes or in peer reviewed journals.

D0 Note # 2281

Proposal to Upgrade the Intermediate & Forward Regions of the D0 Calorimeter

K. De, P. Draper, E. Gallas, R. Kaiser, J. Li, J. Perkins
L. Sawyer, M. Sosebee, R. Stephens, A. White
The University of Texas at Arlington
Arlington, Texas 76019

T. Ferbel, S. Gruendahl, F. Lobkowicz, J. Yu, H. Zhu
The University of Rochester
Rochester, New York 14627

ABSTRACT

We propose to upgrade the D0 calorimeter system by improving the capabilities of the InterCryostat Detector (ICD) and adding a Forward Preshower Detector (FPD). These upgrades are necessary to maintain and enhance the physics capabilities of the D0 detector for Run II. Specifically, the upgrades will preserve hermeticity, provide intermediate EM coverage, and improve electron and photon identification in the forward region. We will explore in this document the motivation and preliminary design for such upgrades which include building a FPD with luminosity capabilities, a new readout for the existing ICD, expanding the ICD to cover showering at the end of the solenoid and building a lead-scintillator EM detector for the intermediate region. Due to extreme constraints on space, money and personnel, we have presented an integrated approach to this region of the calorimeter system.

Contents

List of Tables

List of Figures

List of Abbreviations

ICD – The Intercryostat detector in its current Run I configuration ($0.8 <| \eta |< 1.4$) which samples shower energy after the central calorimeter cryostat walls.

CCMG – The 'massless gaps' which sample shower energy after the 'massive' central calorimeter end plates. They cover $0.7 <| \eta |< 1.2$.

ECMG – The 'massless gaps' inside the end calorimeters which sample shower energy after the end cryostat walls from $0.7 <| \eta |< 1.3$.

ICD^{+} – The proposed extended ICD for Run II covering $0.9 <| \eta |< 1.7$. This detector will play an identical role as the present ICD by providing sampling of energy lost in the cryostat walls (which for Run II will also additionally include the solenoid cryostat walls).

EMICD – The proposed fine sampling multi-layered lead- scintillator detector in the region $1.1 <| \eta |< 1.4$ for Run II. This detector will provide three sampling layers with one or two longitudinal readout depths.

FPD – The proposed forward preshower detector covering $1.8 <| \eta |< 3.0$, which may also serve as a luminosity monitoring device.

LØ – The Level Zero detector as implemented in Run I.

1 INTRODUCTION

1.1 Background

The DØ detector in its current configuration[1] will exist for one more run (Run Ib) at the Tevatron. Substantial changes are planned for Run II, which is scheduled to start in 1997-98. All the central tracking detectors will be replaced. A 2 Tesla solenoidal magnet will be added. Silicon detectors and fiber detectors will be added to provide precise tracking information in the magnetic field. A central preshower detector will be added.

In conjunction with the upgrades to the DØ detector, substantial improvements are also planned for the Fermilab accelerator. The bunch spacing will be reduced to 395 nanoseconds in Run II, and maybe even to 19 or 132 nanoseconds. To accommodate these changes, major upgrades are planned for the calorimeter readout electronics for Run II.

The current status of the DØ Upgrade plans for Run II can be found in Reference 2. Here, we present proposals for additional upgrades to the calorimeter system in the intermediate and forward regions. Some of these upgrades are necessary due to the presence of the new solenoid in the central region. Other upgrades are motivated by our experience with the detector from the first run. All of the upgrades proposed here will significantly enhance the physics capabilities of the Upgraded D0 detector compared to the present design of the detector for Run II.

1.2 Physics Motivations

The primary goals for the intermediate region upgrades are to preserve and improve the hermeticity, uniformity and acceptance of the DØ calorimeter system. Some of the benefits are:

1. **Improved hermeticity** can provide superior measurement of transverse energy (traditionally called missing transverse energy $\not\!\!E_T$). The $\not\!\!E_T$ of an event contains information about the transverse energy carried away by non-interacting neutrinos or possibly by exotic new particles. Good measurement of $\not\!\!E_T$ is important in order to reconstruct events with W decays[3], heavy quark decays[4][5], SUSY decays[6], new massive stable particle production[7] and other such processes.

2. **Improved jet response** in the intermediate region is useful for many of the physics topics currently being pursued with Run Ia data. For example, rapidity gap studies rely on uniform sensitivity over a large rapidity range of the detector[8]. Compositeness searches require accurate measurement of total scalar E_T in a multi-jet environment[9]. In addition, any physics process which produces multiple jets (for example, top decays[4]), would suffer from low efficiency if fiducial cuts were made in the intermediate regions of the detector.

3. **Adding electron identification** in the intermediate region will substantially increase the accepatnce and efficiency for many physics processes including top search[4], SUSY searches[6], electroweak physics and signals for physics beyond the standard model. In addition, fake backgrounds due to the misidenfication of electrons can be reduced.

Upgrades to the forward region are motivated by two considerations – (1) increased efficiency for forward physics processes and (2) accurate luminosity measurement. A highly segmented forward detector can enhance photon and electron identification. Measurement of gluon structure functions can be improved significantly by studying direct photon production at large rapidity[10]. Improved electron identification will benefit heavy quark physics[5] and new particle searches – in fact, almost all physics processes which need EM information will benefit from the increased acceptance. In addition, new physics topics like W/Z asymmetry[11] can be explored.

The accurate measurement of live luminosity is essential for all cross-section measurements, including the ability to set limits for new physics processes. Currently,

the LØ detector performs this function[12]. We explore the possibility of using the forward preshower detector, proposed here, for this task.

1.3 Hardware Considerations

The DØ liquid argon calorimeter system is contained in three separate cryostats. The central cryostat (CC) provides complete electromagnetic and hadronic sampling in the pseudorapidity ($\eta \equiv -\ln\tan(\theta/2)$) region $-0.8 < \eta < 0.8$. The end cryostats (EC) provide full sampling in the region $1.4 <\mid \eta \mid < 4.0$. The intermediate region $0.8 <\mid \eta \mid < 1.4$ is covered partially by modules in the central cryostat and partially by overlapping modules in the end cryostats.

Due to the triple-cryostat design of the DØ calorimeter, there is substantial unsampled material in the intermediate region, which degrades energy resolution. In order to solve this problem, additional layers of sampling are introduced in DØ between the cryostats. One layer is inside the central cryostat and is called the central cryostat massless gaps (CCMG). Another layer is inside the end cryostat and referred to as the end cryostat massless gaps (ECMG). A third layer of scintillator sampling used between the cryostats is called the intercryostat detector (ICD). An elevation view of the present DØ calorimeter and the central detector systems is showed in Figure 1. The three additional layers in the intermediate region help provide a hermetic and uniform calorimeter system for DØ.

The scintillator based ICD uses photomultiplier tubes (PMT) to convert light pulses to electronic signals. These PMTs will not work after the introduction of the solenoid in Run II. It is essential to upgrade the PMT readout so that the ICD functionality is preserved in Run II.

There will be additional unsampled material in Run II at the ends of the solenoid cryostat. We propose to provide scintillator sampling to recover this lost energy by extending the ICD.

The DØ detector has missing or incomplete electromagnetic coverage between

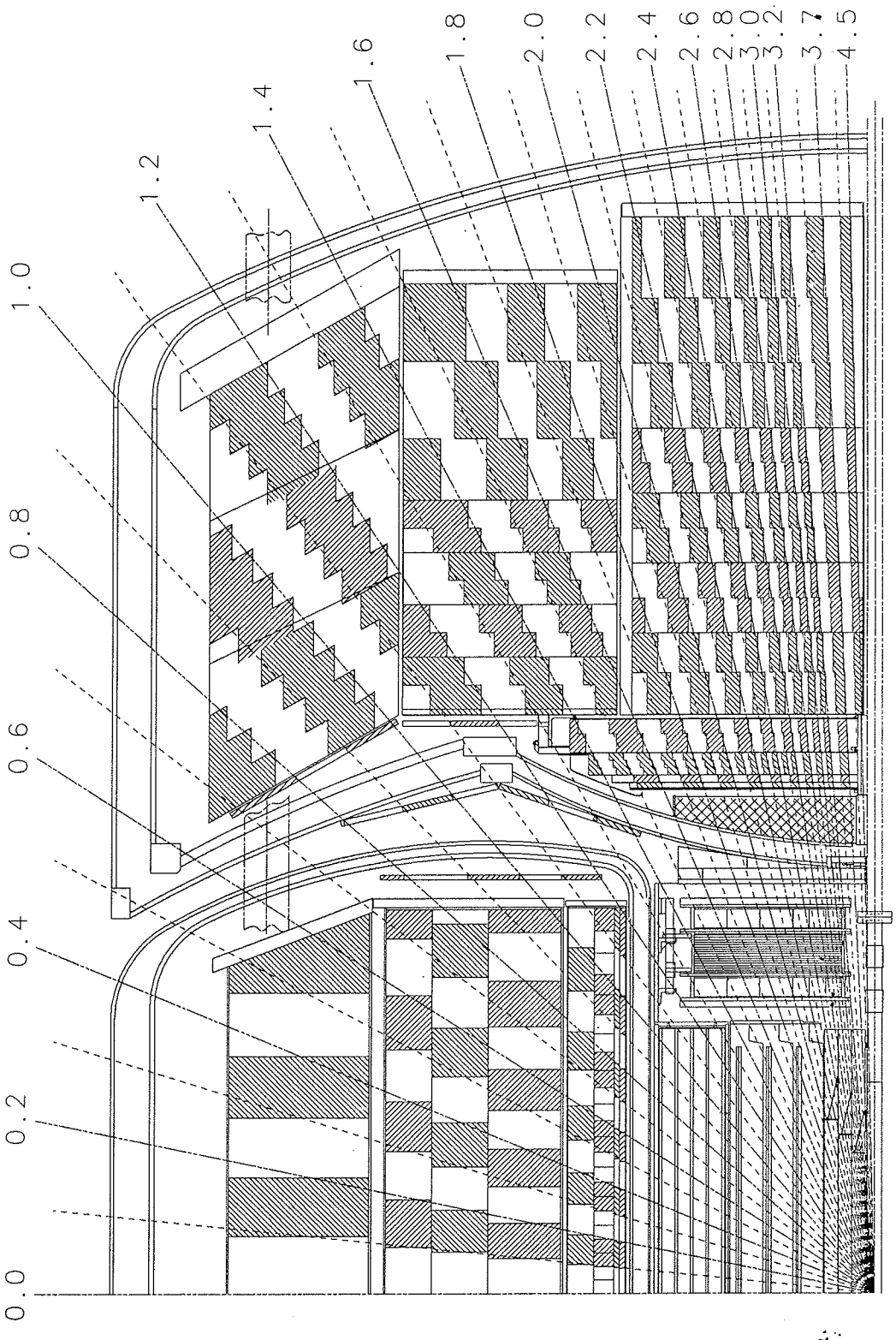

Figure 1: Elevation view of one quarter of the DØ calorimeters showing cell boundaries in the yz plane. The radial lines emanating from the collision point are labelled in units of η.

$1.1 <| \eta |< 1.4$. Primarily, coarse hadronic sampling is available in this region, thereby making it impossible to identify electromagnetic showers or measure their energy accurately. We propose to build a longitudinally segmented sampling detector in this region.

A preshower detector for the barrel region is planned for Run II. In the past, the PAC has encouraged DØ to study the possibility of adding a FPD. This detector can help with electron and photon identification, especially for low momentum particles. We explore here the basic design needs for such a detector.

Currently, the LØ detector provides luminosity information using a scintillator based detector in the forward region. In considering the design of the forward preshower detector which will overlap the region covered by the current LØ detector, we plan to explore the feasibility of using it as a luminosity monitoring device.

Due to the adjacent regions in η covered by all the above upgrades, and the extreme space constraints in the intermediate regions, we propose here an integrated approach to the detectors mentioned above. Even though it might be necessary to separate the final detector into 2-3 pieces, installed at different times, we need to consider their design, development and implementation in an integrated fashion. A side view of all the proposed upgrades is shown in Figure 2.

In summary the following three detectors are proposed:

1. An expanded ICD in the region $0.9 <| \eta |< 1.7$ to sample energy after the central cryostat and solenoid cryostats, thereby improving uniformity and hermeticity of the calorimeter system.

2. A new electro-magnetic sampling calorimeter called EMICD in the region $1.1 <| \eta |< 1.4$ to reconstruct and identify electrons.

3. A forward preshower detector in the region $1.8 <| \eta |< 3.0$ to help electron and photon identification and triggering.

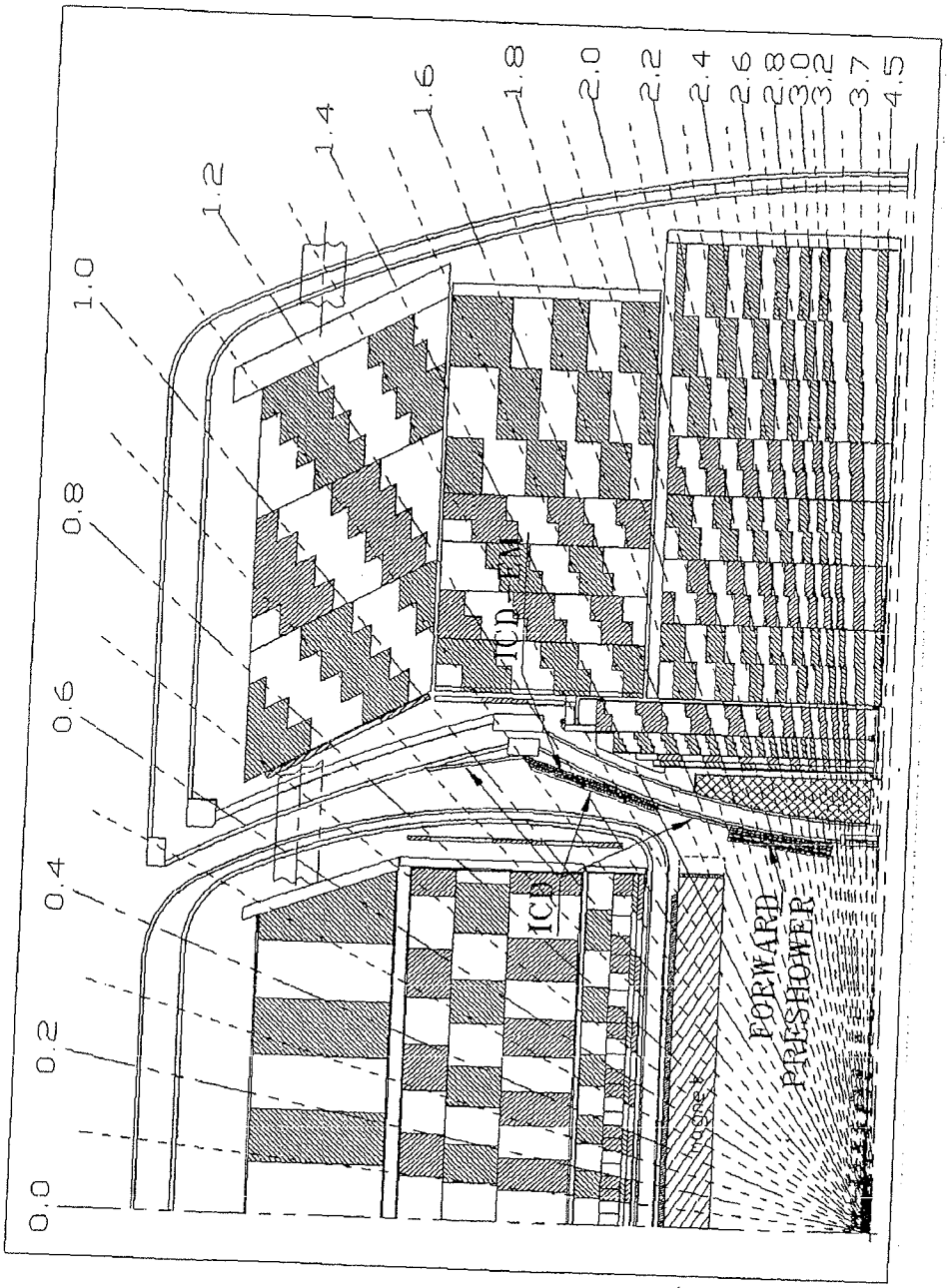

Figure 2: Side view of ICD, EMICD and FPD detectors

It is worth emphasizing here the importance of upgrading the forward tracking detectors in order to take full advantage of the forward preshower detector proposed here. Both electron and photon identification rely heavily on the existence or absence of particle tracks connecting up to the preshower energy deposition. Tracking is also necessary to determine the charge of leptons in the forward region. In writing this proposal, we assume that a minimal forward tracker is part of the upgraded DØ detector for Run II.

2 The ICD$^+$ SOLUTION

2.1 The Old ICD

As mentioned above, the orginal ICD, as implemented currently in DØ is a scintillator based shower detector mounted on the face of the end cryostats. Covering the pseudo-rapidity range $0.8 <| \eta |< 1.4$, the ICD helps to improve energy measurement and energy resolution in the intermediate region of the DØ calorimeter. It comprises of 768 channels, with a 0.1×0.1 segmentation in η and ϕ (azimuthal angle). Each channel is composed of a scintillator plate, wave- shifting fibers, PMT, voltage divider, charge integrating amplifier, digitization electronics, charge pulser, laser pulsing system and readout electronics.

The scintillators, PMTs, voltage dividers and preamps are mounted inside 256 boxes covering the faces of the two end cryostats. Power distribution patch panels, pulser fanouts and other electrical support systems are placed in racks underneath the detector. Readout of the electrical signals is integrated as part of the liquid argon calorimeter ADC-BLS readout system. A laser calibration system is implemented in the moving counting house.

Due to the restricted space between the cryostats, a compact design for ICD tiles was required and achieved by use of flexible bundles of wavelength shifting fibers epoxied into grooves in scintillator plates. These fiber bundles transport the scintil-

lation light from the tiles to small PMTs for conversion to an electrical signal which are then digitized.

The hermeticity and uniformity of the DØ calorimeter may be best illustrated by looking at jet-photon transverse energy balance from collider data. I use a preselected sample of well measured direct photon candidate events. The events are chosen to contain one additional jet only. The jet and the photon are constrained to be back-to-back in ϕ within 0.4 radians. Then the asymmetry variable can be defined as:

$$A = \frac{E_T^j - E_T^p}{0.5 * (E_T^j + E_T^p)}.$$

A should be constant as a function of η for uniform calorimeter energy measurement. The the width of the distribution of A is a function of the jet energy resolution. In Figure 3, we plot the asymmetry distribution as a function of the pseudo-rapidity angle of the jet, with and without the energy measured in the ICD and the massless gaps. This figure shows that when the energy sampled in the ICD and the massless gaps is removed, there is substantially less energy measured in the inter-cryostat η region using default liquid argon calorimmeter sampling weights. Some of this energy might have been recovered by tuning the sampling weights in the rest of the calorimeter, but at the expense of poor resolution.

2.2 The New ICD$^+$

The jet-photon asymmetry plot shown in Figure 3 was generated from Run I NTUPLEs which only contained information about the combined contribution from the ICD and MG to the total jet energy. While this plot might be used to show how well we did in Run I by implementing the ICD and MG detectors, it is not very useful for optimizing the design of the ICD for the upgrade. In order to study the individual contribution from the ICD to calorimeter energy resolution, we have performed a new study using test beam data. For this study, we started with the default sampling weights currently used in DØ and applied them to test beam data from 100 GeV pions. This provides a control sample representing the current DØ detector. Next,

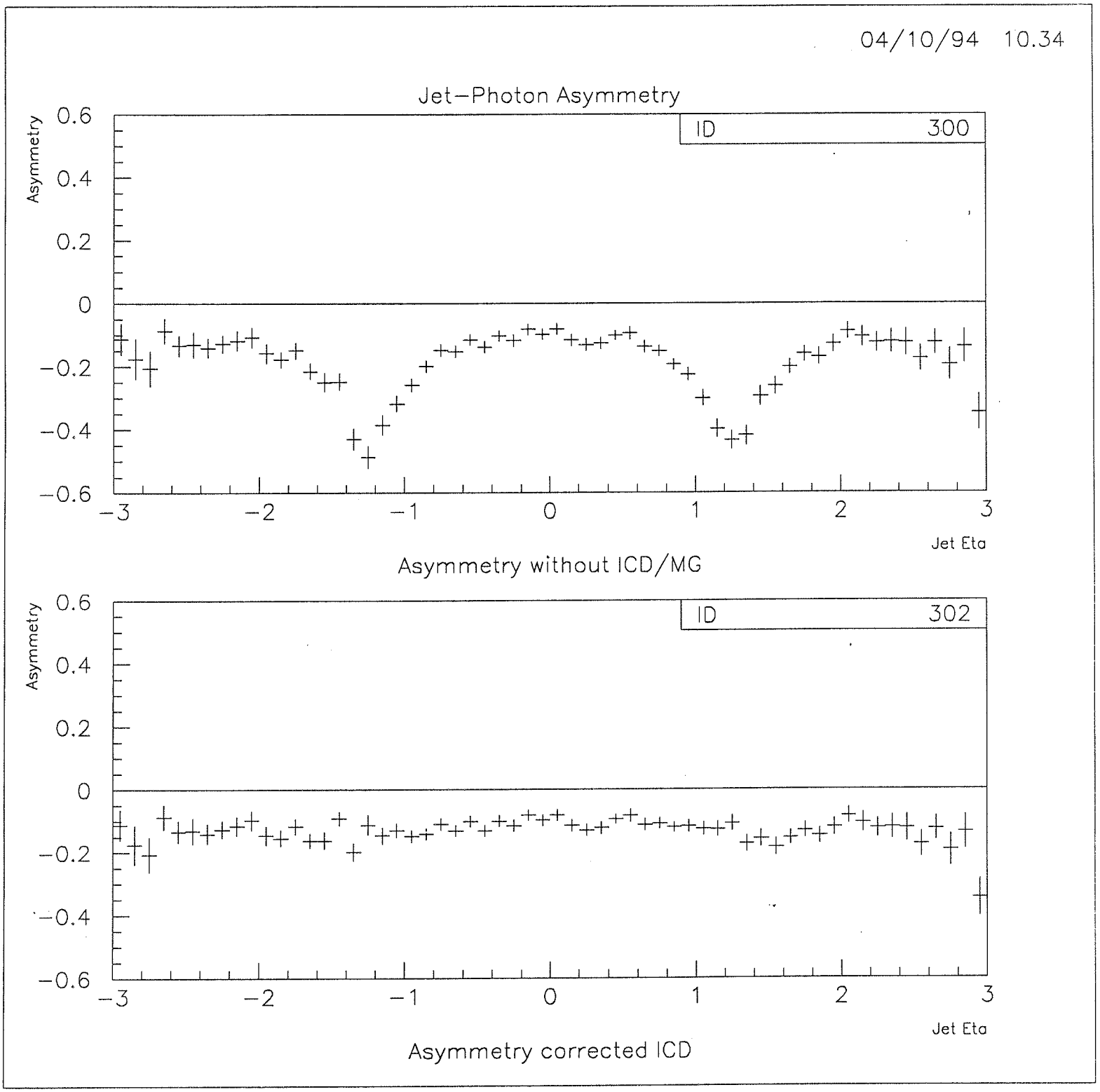

Figure 3: Improvement in Jet-Photon Asymmetry due to ICD/MG

we set the ICD sampling weights to zero and reoptimized the CC and EC massless gap sampling weights. Processing the same test beam data using this new set of sampling weights will show the best possible calorimeter response if the ICD were never implemented. In Table 1 we show the default DØ sampling weights (SW) for the ICD and MG. The newly optimized sampling weights without the ICD are shown

Eta	CCMG SW	ICD SW	ECMG SW
0.85	4.014	37.28	2.116
0.95	4.995	25.04	3.094
1.05	4.536	34.29	3.151
1.15	6.675	34.92	4.743
1.25	0.000	69.65	2.357
1.35	0.000	57.39	0.000

Table 1: Default sampling weights used in DØ for Run I.

in Table 2. Note that the EC and CC massless gap sampling weights increase by

Eta	CCMG SW	ICD SW	ECMG SW
0.85	7.631	0.000	3.978
0.95	7.892	0.000	6.460
1.05	7.530	0.000	4.197
1.15	11.73	0.000	5.750
1.25	0.000	0.000	5.270
1.35	0.000	0.000	0.000

Table 2: Re-optimized sampling weights after excluding ICD.

about 50% each in response to the missing ICD. For $\eta = 1.25$, where only the ECMG is available, the sampling weight increases by almost a factor of two when the ICD is removed.

In Figure 4a we show the energy distribution from 100 GeV pions at the DØ Test Beam for $\eta = 1.25$ without the ICD sampling, using the reoptimized sampling weights shown above. The energy distribution is not Gaussian and has very poor energy resolution. The addition of the ICD sampling dramatically improves the energy mea-

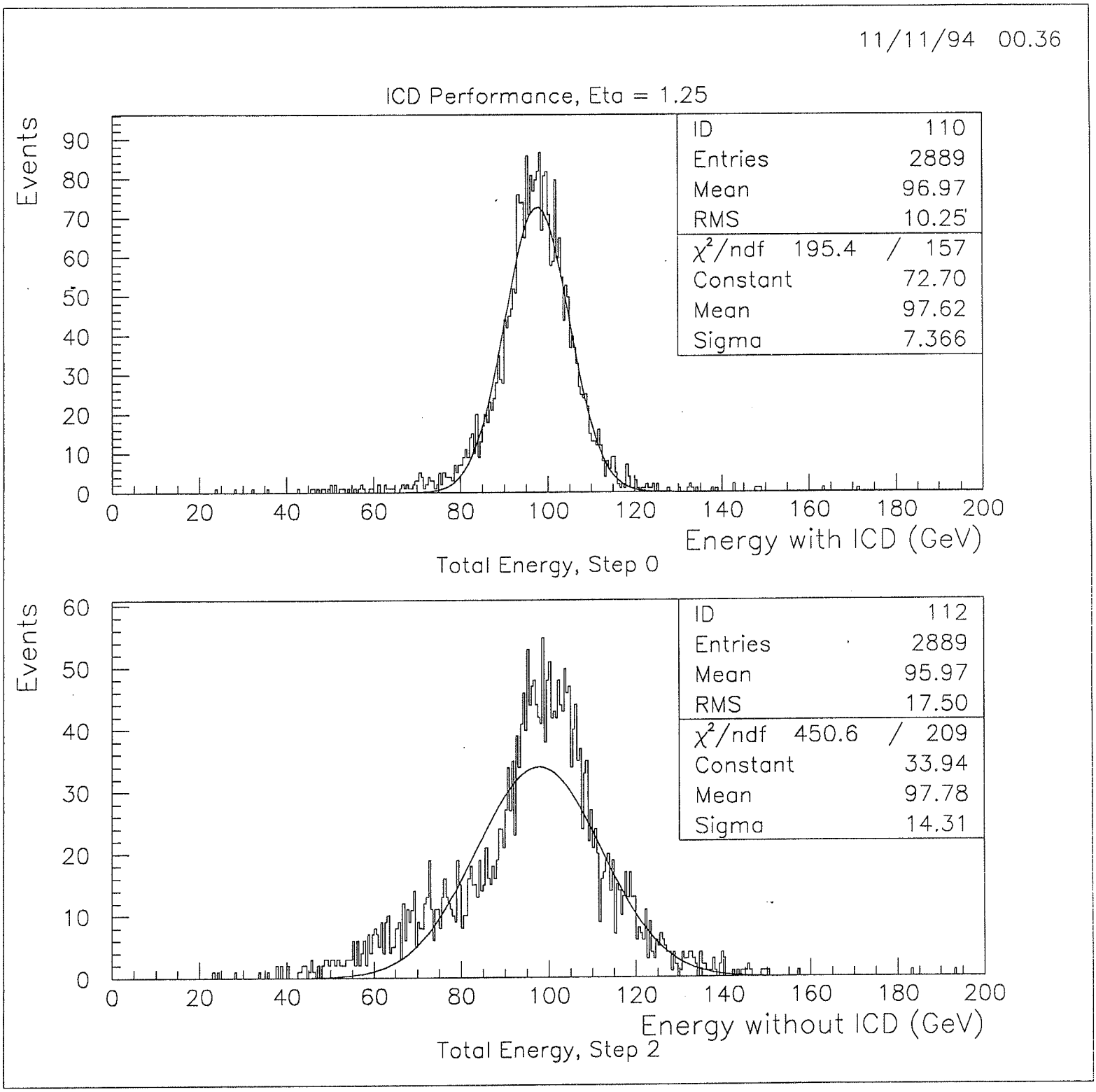

Figure 4: Effectiveness of ICD Sampling for $\eta = 1.25$

surement, as shown in Figure 4b. We see similar results in Figure 5 for $\eta = 1.35$. For $\eta = 1.15$, shown in Figure 6, the effect of the ICD is not so obvious. The width of the resolution is dominated by the un-sampled material in the stiffening ring of the end cryostat. We are currently reoptimizing the sampling weights to obtain better resolutions. We expect that the ICD contribution will be more obvious when the resolution gets better.

Figure 7 for $\eta = 0.85$, Figure 8 for $\eta = 0.95$, and Figure 9 for $\eta = 1.05$ show the effect of removing the ICD in the low η region. The energy resolution improves about 10-15% in this region by adding the ICD. The non-gaussian tails of the distributions, especially above the mean is increased in some cases. These tails can give rise to substantial missing E_T. Therefore, it is essential to maintain the ICD for Run II so that the DØ calorimeter remains hermetic and uniform.

The ICD samples very little energy in the region $0.8 <| \eta |< 0.9$ due to the many interaction lengths present in the CC before the ICD. As shown above with test beam data, the non-gaussian tails are not terrible without the ICD even though the energy resolution (width of the distribution) improves by about 15%. Therefore, we propose to eliminate ICD coverage in this region for the upgraded detector. However, we need to expand the ICD coverage into much higher pseudo-rapidity regions in order to sample the showers created in the solenoid cryostat walls.

The pseudorapidity range corresponding to the flat end of the magnet cryostat bulkhead extends from $\eta = 1.41$ to $\eta = 1.67$ ($\theta = 0.37$ to $\theta = 0.49$ in radians). In order to overlap the material in the cryostat, the new ICD$^+$ detector will cover $0.9 <| \eta |< 1.7$. This requires expanding the current coverage by 30% – from 768 channels to 1024 channels.

2.3 Readout Choices

The biggest R&D challenge in designing a new ICD is to develop a new photon detection scheme which will operate in the high magnetic fields. There are four

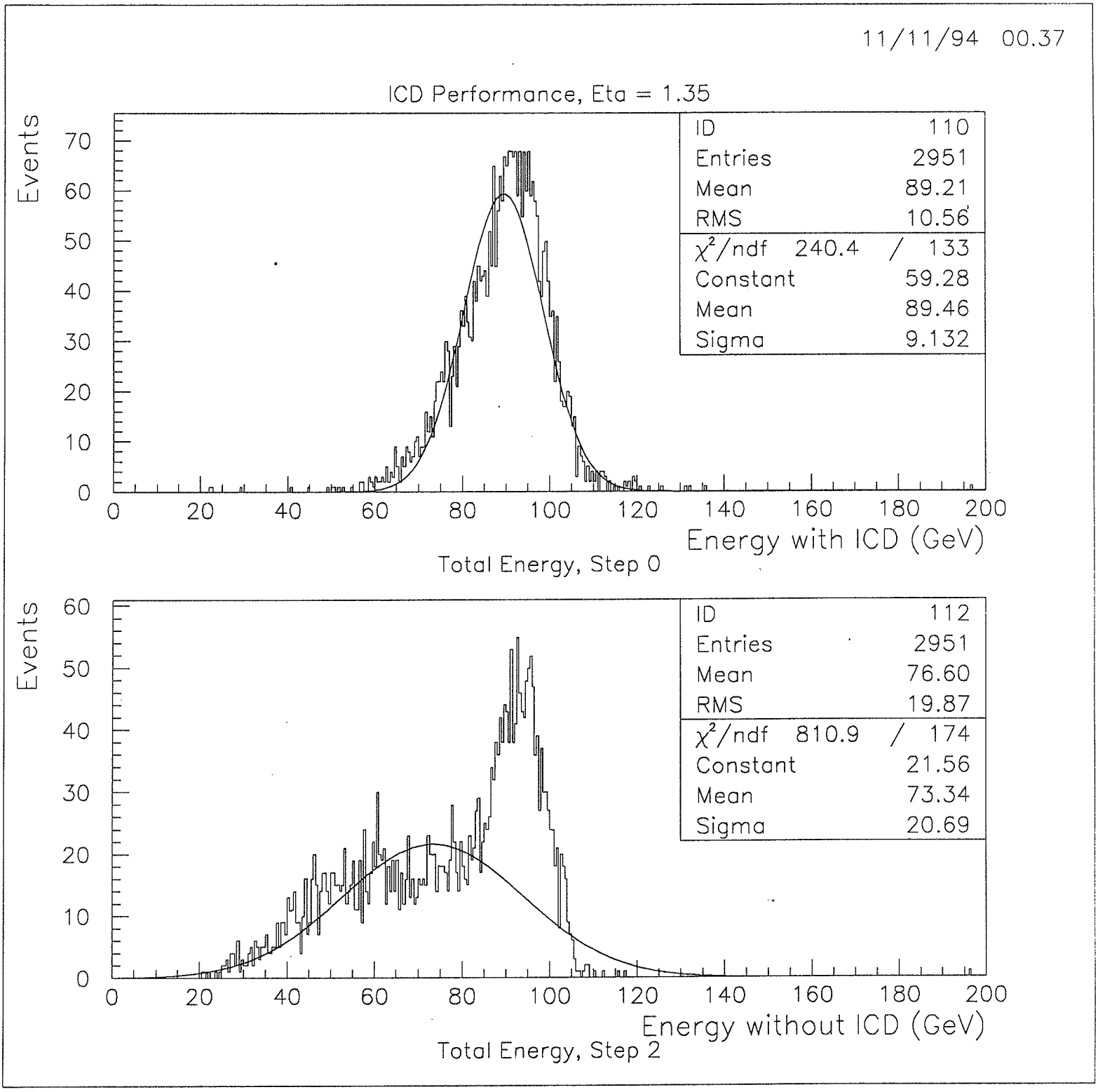

Figure 5: Effectiveness of ICD Sampling for $\eta = 1.35$

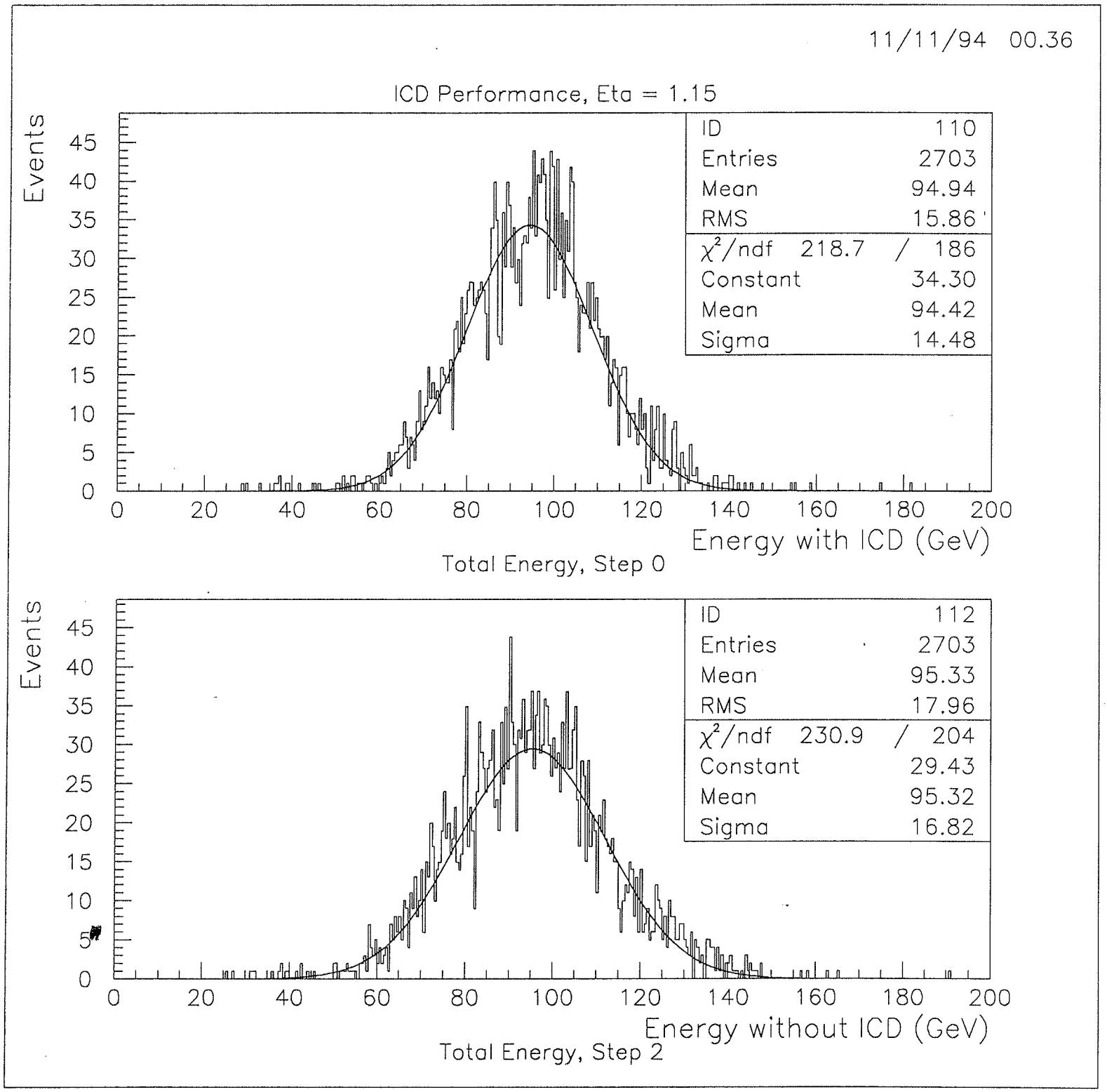

Figure 6: Effectiveness of ICD Sampling for $\eta = 1.15$

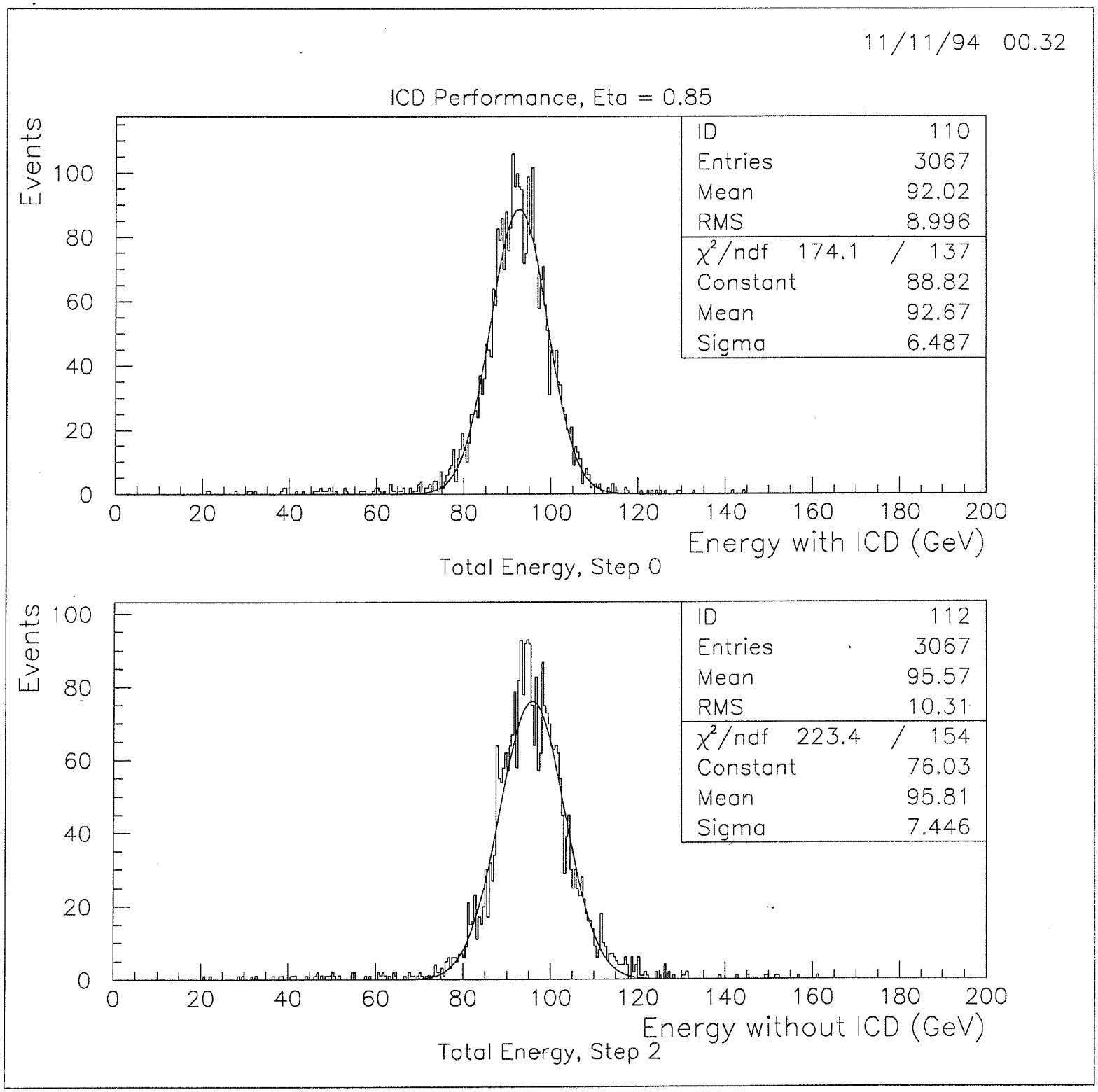

Figure 7: Effectiveness of ICD Sampling for $\eta = 0.85$

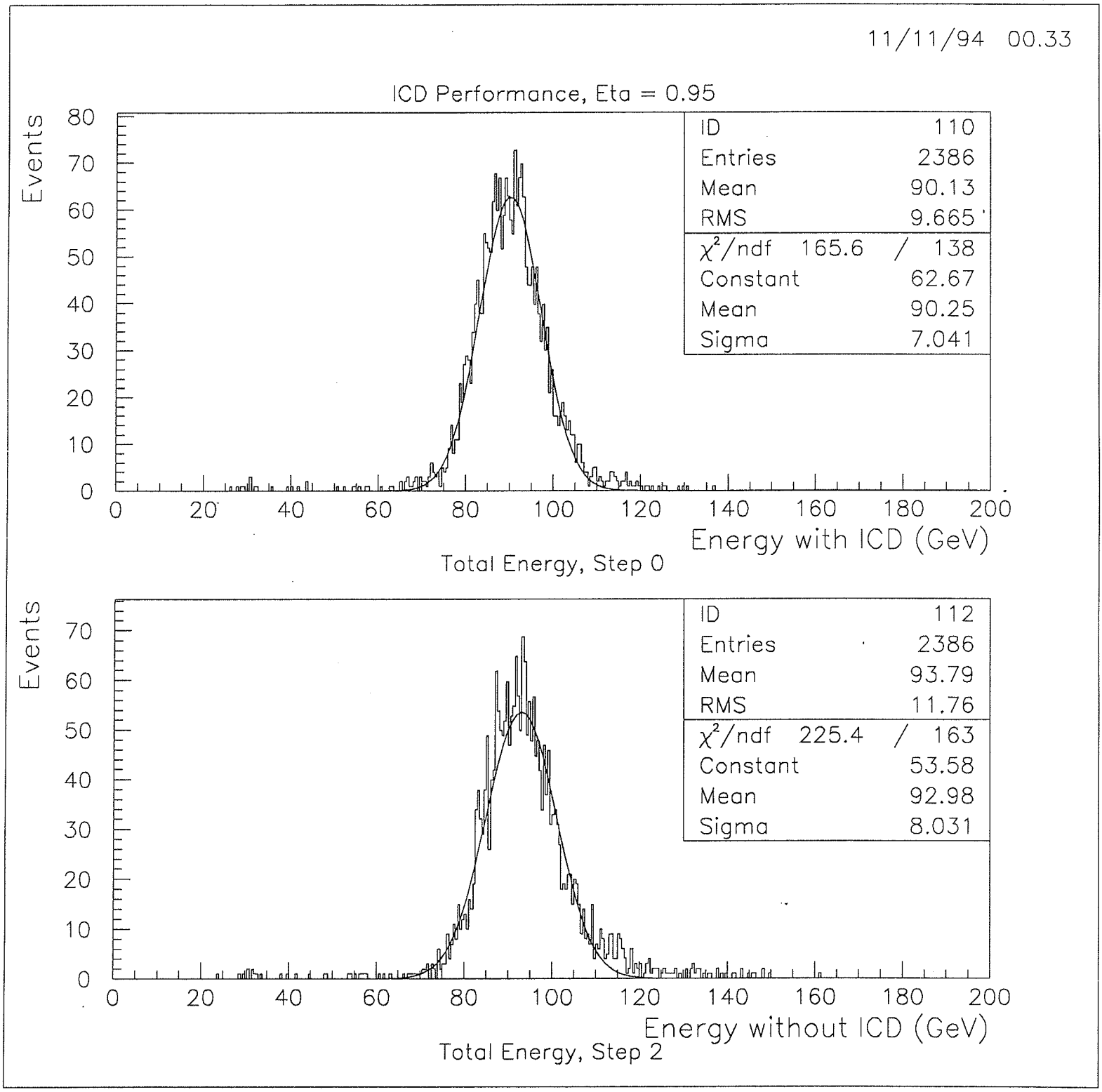

Figure 8: Effectiveness of ICD Sampling for $\eta = 0.95$

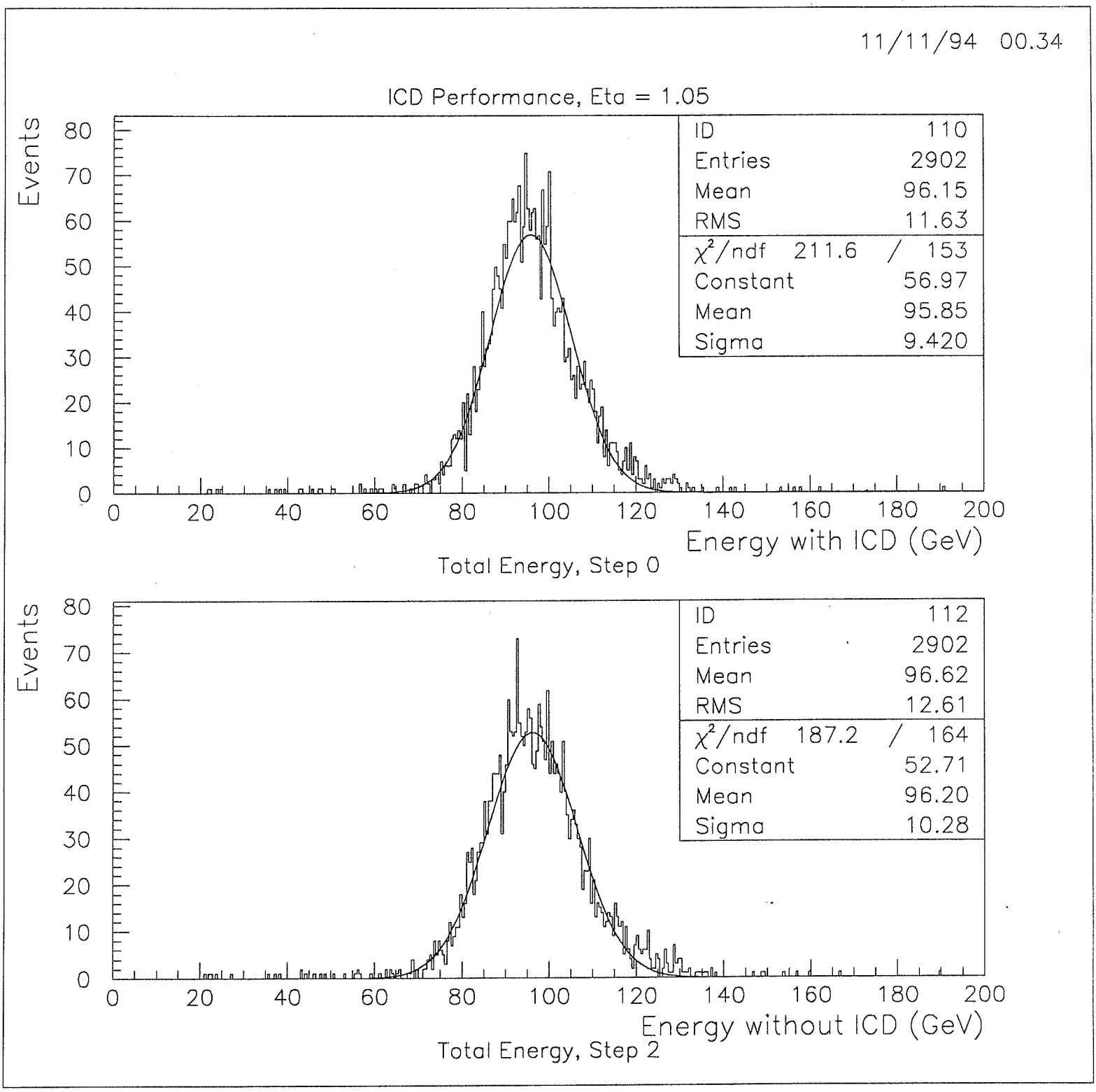

Figure 9: Effectiveness of ICD Sampling for $\eta = 1.05$

distinct options we are considering.

1. Replacing the PMTs with avalanche photodiodes (APD). The APDs are commercially available and immune to magnetic field effects. However, they are still expensive, provide smaller active area, have lower gain but higher quantum efficiency, and generate higher noise. We are currently testing Hamamatsu APDs to evaluate their performance at low light levels. Using a LED pulser, high gain preamplifiers and postamplifiers, we have measured them to be linear from about 30 to 30,000 photoelectrons. In the future, we will use cosmic ray signals to benchmark the APD tests against other photodetectors.

2. Replacing the PMT's with new ultra-compact Hamamatsu R5600 series PMT's. These PMTs use mesh dynodes which are resistant to magnetic fields. We have obtained two of these new tubes. Preliminary tests show that even though they are noisier than traditional PMTs, the signal to noise is adequate for use in the ICD upgrade. Further tests are needed to quantify their resistance to magnetic fields.

3. Moving the PMTs to a region where the magnetic field strength is acceptably low. Currently, the PMTs, bases, and preamplifiers are all situated on top of the scintillators inside a common aluminum enclosure housing 3 ICD channels. We can redesign the ICD such that the light can be transported via 2-3 meter long fibers to the PMTs which can then be situated in a low magnetic field region. At the test beam we successfully used 3 m long fibers to transport the scintillator light out of the liquid argon cryostat[25]. This is our backup option since it uses proven technology. However there are difficulties in implementation due to the limited availability of space near the calorimeters.

4. Using visible light photon counters (VLPC) instead of PMTs. The tracking upgrade of the DØ detector will use VLPCs and they are currently being evaluated by DØ. Since VLPCs require cryogenics support, they are technically challenging to implement. Their dynamic range might be too small for use in the ICD. However, we plan to test their feasibility for possible use in the ICD.

Our backup plan is to use PMT's. About half the number that we need can be recycled from the present ICD. In order to allow operation in the solenoidal magnetic field, we propose to move the PMTs to a region where the field strength is tolerable. Clear fibers will be used to transmit the light from the scintillator tiles to the remote PMTs. At the DØ Test Beam we used 3 meter long fibers with better than 90% efficiency successfully. We plan to use a similar approach for the upgrade.

The PMTs used in the current design of the ICD have been tested in fields up to 200 Gauss with no effect independent of orientation. We plan to add more shielding in order to survive a field of 300 Gauss. As seen in the field map, there are potential regions within 3-5 meters of the location of the ICD where the PMTs may be placed safely with the added shielding.

We propose to use the existing ICD electronics and digitization channels in order to reduce cost. We will need to increase the number of channels by an additional 30%. The additional capacity exists in the current ADC-BLS system and can be used with minimal rewiring.

Reliable fiber readout is key to the success of this design. In order to maintain fiber interface integrity, the readout fibers should be ganged in convenient groupings to the closest connector in that quadrant or octant. The modularity of the current ICD design has proven to be very useful because it is possible to remove and service individual ICD boxes without disturbing the others. Each box in the current design covers 0.1 in azimuth. We propose to build the ICD$^+$ detector in groups of 0.4 in azimuth to reduce cost.

2.4 Conclusion

We propose to build an expanded ICD which will operate in the solenoidal magnetic field of the upgraded DØ detector. The expanded coverage is necessary to sample showers after the new solenoid cryostat. We have embarked on an R&D effort to evaluate the performance of various photodetector options. We are also studying

various prototypes of scintillator tiles. A budget and schedule for the project is appended at the end of this document.

3 EMICD

3.1 Missing Electrons

We were able to successfully treat the problem of poor energy measurement in the intermediate region with the ICD and the MGs. However, this did not solve the problem of poor electron identification in the intermediate region. There exists a hole in electron reconstruction efficiency in the pseudorapidity range $1.1 <| \eta |< 1.4$. This hole is due to the absence of EM sampling layers. In this region, electron energies are also poorly measured because of energy loss in the cryostat walls and other unsampled absorbers.

This "EM hole" can be seen in any plot of electron psuedorapidity for the current DØ detector, whether in Monte Carlo or data. For example, Figure 10 shows the eta distribution of electrons in $t\bar{t}$ Monte Carlo signal events. Even though the physical extent of this hole is $1.1 <| \eta |< 1.4$, the loss of acceptance for physics processes is much greater, since most analyses make a fiducial cut for electrons in the range $1.0 <| \eta |< 1.5$ to avoid edge effects.

The absence of EM layers in the intermediate region also creates non-uniformities in other physics topics which may not specifically require electron identification. For example, low energy jet response becomes nonlinear due to the mismeasurement of the soft π^0s. Trigger efficiencies are significantly lower since a much smaller fraction of the tower energy is sampled. Rare particle searches have to contend with non-uniform response.

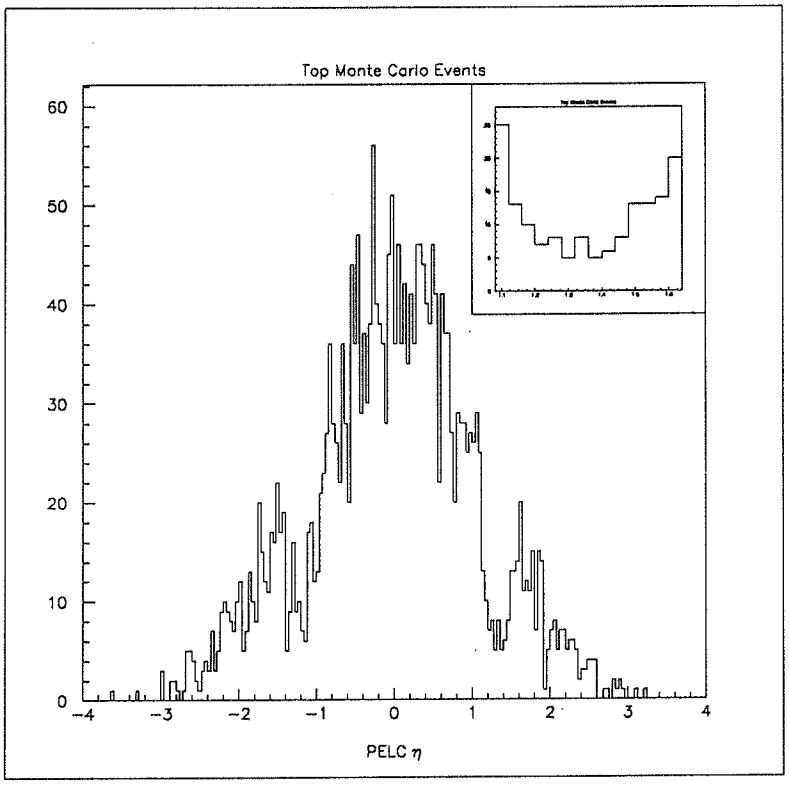

Figure 10: Eta distribution of reconstructed electrons in $t\bar{t}$ Monte Carlo events, showing acceptance losses in the EM hole near $\mid \eta \mid = 1.3$. The inset shows an expanded view of the hole.

3.2 Physics Studies

In order to understand the electron inefficiencies, we studied a sample of Monte Carlo electrons in the intermediate region, using D0GEANT. Single electrons with 50 GeV energy were generated in the region from $1.0 <| \eta |< 1.6$. There were 160 electron in each 0.1 segment in η. These single electron events were then processed through the reconstruction program and the number of physics objects were histogrammed, as shown in Figure 11. Very few reconstructed electrons are found in $1.1 <| \eta |< 1.2$, while none are found in $1.2 <| \eta |< 1.4$. The inefficiency in electron identification is due to the missing EM layers in the liquid argon calorimeter. Some of these electrons are reconstructed as jets with mismeasured energies.

The misidentification of electrons and mismeasurement of their energies directly impacts physics analyses:

- Missing transverse energy resolution is degraded in events with electrons in this region since the electron energy is mismeasured;
- Background rates for rare searches are increased since backgrounds with known topologies which might produce an electron in the intermediate region ($W, Z, t...$ decays) cannot be identified and therefore produce fake signal events;
- There is a substantial loss of acceptance for inclusive electron processes, especially for processes which include multiple electrons.

ISAJET studies were carried out for a number of physics processes containing electrons in the final state. These studies assumed that any electron in $1.1 <| \eta |< 1.4$ is lost in the reconstruction. All electrons were required to have $P_T > 10$ GeV. The results are summarized in Table 3.

Clearly the likelihood of losing an electron in the EM hole goes up with the electron multiplicity in the final state. There is roughly an inefficiency of 10%/electron (ignoring differences in the eta distribution of higher mass particles, P_T distributions,

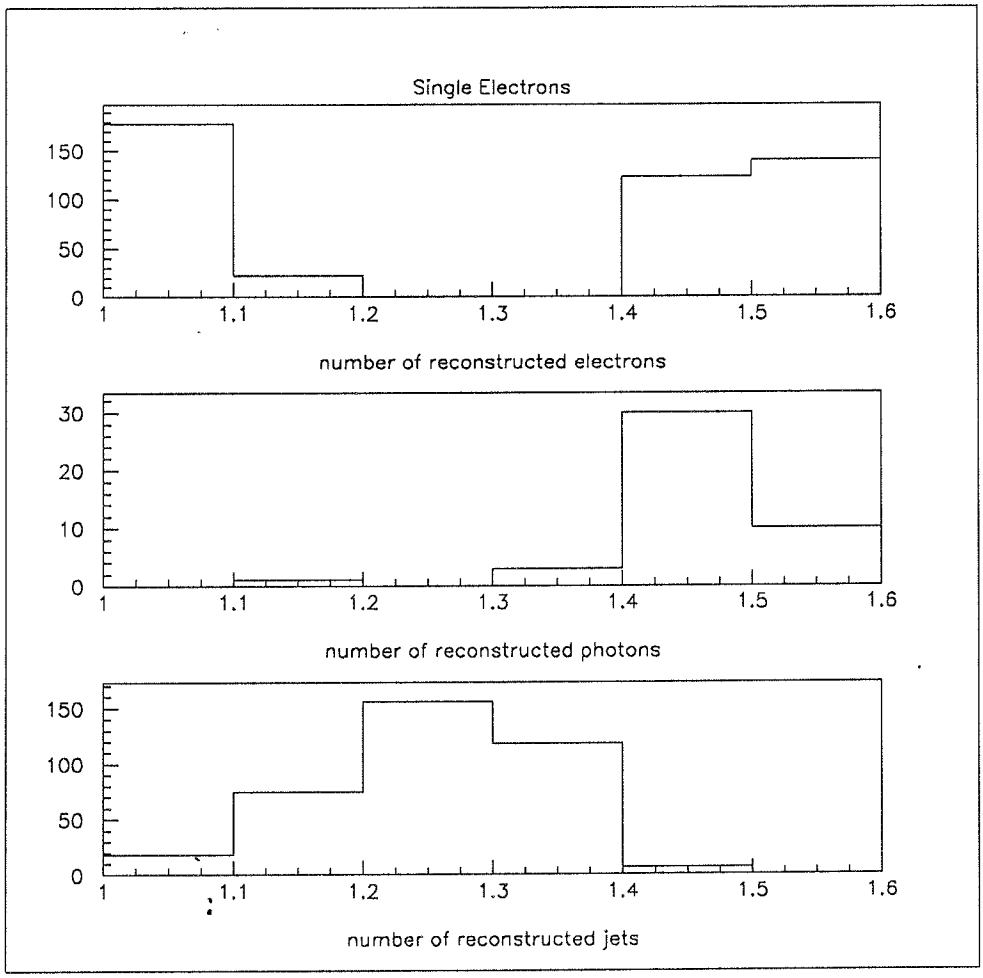

Figure 11: Reconstructed objects in the region from $1.0 < |\eta| < 1.6$, for single electron Monte Carlo events and the Run 1 DØdetector. (There were initially 160 electrons per eta bin.)

Physics Process	Percentage of events with 1 or more electrons in $1.1 <\mid \eta \mid < 1.4$
$t\bar{t} \rightarrow e + X$	9.9 ± 0.6 %
$W \rightarrow e\nu$	11.5 ± 1.2 %
$Z \rightarrow e\bar{e}$	21.1 ± 1.6 %
$\tilde{W}_1\tilde{Z}_2 \rightarrow eee$	20.8 ± 3.0 %

Table 3: Electron losses for various physics channels, from ISAJET simulations.

etc.). Eta distribution of electrons in these ISAJET events are shown in Figure 12. As mentioned before, the actual loss is even greater since most analyses make fiducial cuts in the region $1.0 <\mid \eta \mid < 1.5$ to avoid edge problems. This typically adds another 5-10% to acceptance losses.

The EM hole can also cause large backgrounds to rare searches. In the traditional search for supersymmetric particles at hadronic colliders, one looks for large missing E_T in association with jet activity[6]. When the electron from a W decay is misidentified as a jet in the EMICD region, the large missing E_T from the neutrino in the decay becomes background to the SUSY search. In Figure 13 we show the eta distribution of jets in events with large missing E_T after some of the cuts used in the SUSY search were applied. The peak in the EMICD region corresponds to the background from W decays.

Events with two electrons and multiple jets provide a promising new channel to search for SUSY particles. We generated events with $m_{\tilde{g}} = 300.0$ GeV, $m_{\tilde{q}} = 310.0$ GeV, $\tan\beta = 2.0$, and $\mu = -500.0$. In Table 4 we show the increase in acceptance for various incremental addition to electron identification with new detectors. The increase in acceptance for all these topics provide a strong motivation for considering a new detector to cover the 'EM hole'.

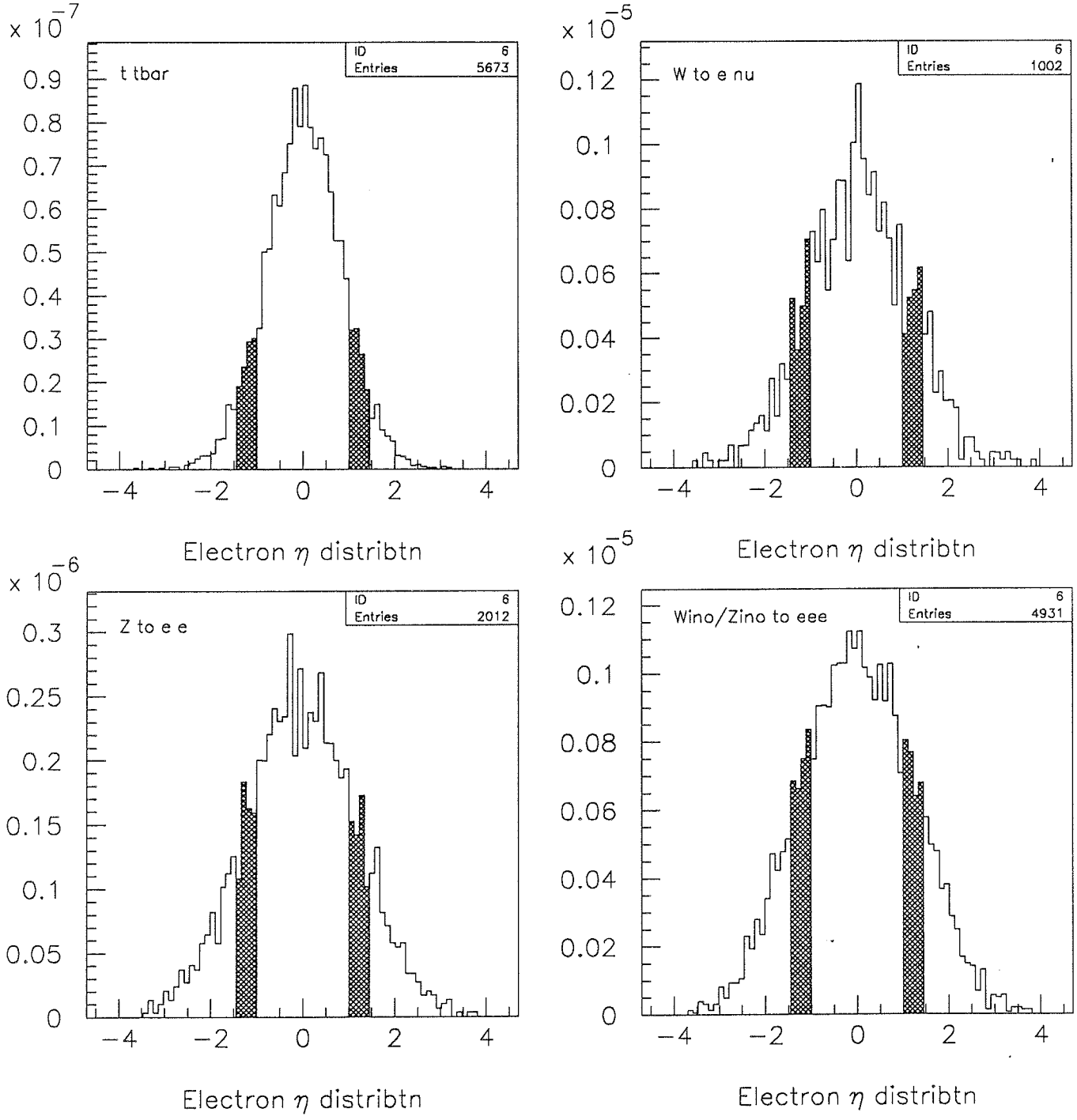

Figure 12: Eta distributions of electrons in ISAJET for the following physics processes : $t\bar{t} \rightarrow e + X$, $W \rightarrow e\nu$, $Z \rightarrow e^+e^-$, and the SUSY process $\tilde{W}_1\tilde{Z}_2 \rightarrow eee$ ($M_{\tilde{W}_1} = 56\tilde{\text{G}}\text{eV}$). The region $1.1 < |\eta| < 1.4$ is shaded in each plot.

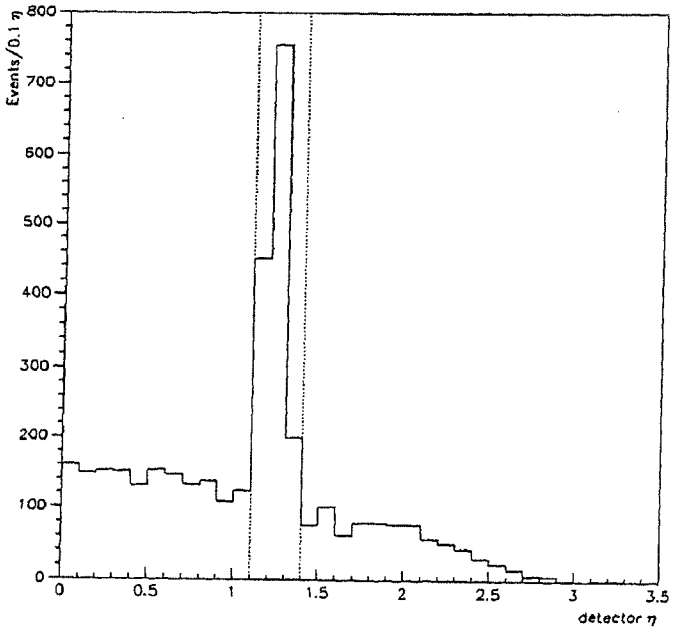

Figure 13: The η distribution of jets in events with large missing E_T showing excess from misidentified $W \rightarrow e\nu$ events.

Fiducial Boundary in eta	Events Accepted 2 electrons,$p_T \geq 10$	Events Accepted 1 e,$p_T \geq 20$+1 e,$p_T \geq 5$
-1.0 – 1.0	68.6%	66.2%
-1.4 – 1.4	86.8%	85.7%
-2.5 – 2.5	99.6%	99.8%
-4.0 – 4.0	100.0%	100.0%

Table 4: Increase in acceptance for SUSY searches as a function of the η coverage of the upgraded detector

3.3 GEANT Studies

We propose to restore the electromagnetic sampling in the region $1.1 <| \eta |< 1.4$ by adding a sampling EM calorimeter behind the ICD. We have begun preliminary Monte Carlo studies of the effect of adding an EMICD between the cryostats. In our first attempt, a new detector volume was added to the upgrade version of D0GEANT (usually referred to as UPG_GEANT), which replaces the current ICD in the η region 1.1-1.4. This volume is implemented in a fashion similar to the existing ICD. Studies were carried out assuming 3 successive layers of lead and scintillator. Single electron simulation with this new detector volume clearly demonstrated that, while there was better energy resolution and an improved longitudinal shower profile for the electrons, there was still a loss of reconstructed energy due to losses in the upstream CC cryostat wall. In other words, we will still need an additional scintillator sampling (an ICD) in front of the EMICD.

After modifying the geometry to include an ICD (a layer of scintillator in front of the EMICD with independent readout of the signal), the UPG_GEANT studies were repeated. We have calculated new optimized sampling weights for the ICD/MG in the new geometry and have used these optimized weights for all energy calculations. The electron identification efficiency can be demonstrated by looking at the fraction of energy deposited in the new detector by electrons and pions. In Figure 14 we plot the EM energy fraction for 50 GeV electrons. The EM fraction for electrons is peaked near 1, as expected for EM calorimeters. The hadronic response, which includes all

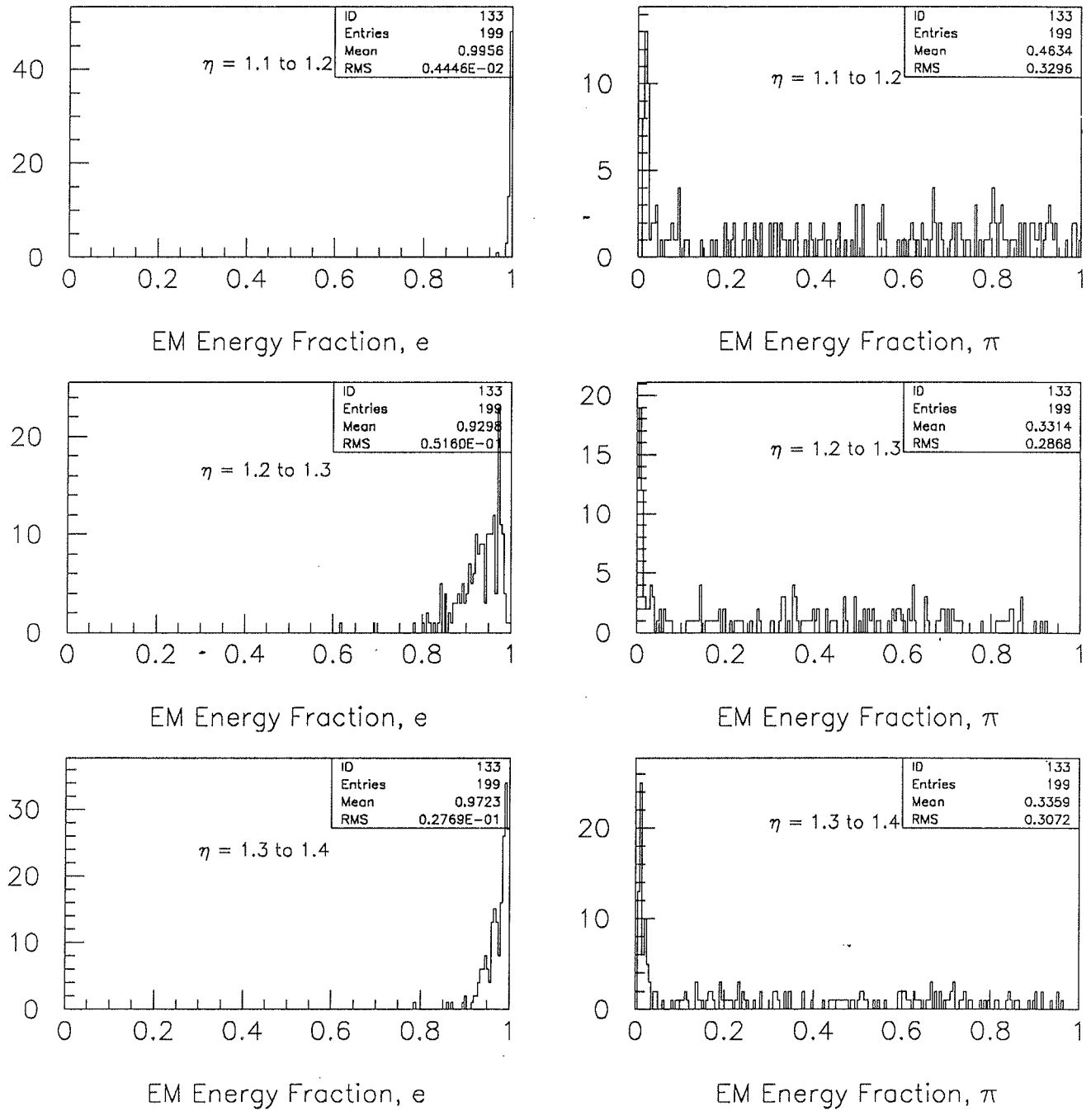

Figure 14: The electro-magnetic energy fraction of e and π showers in different regions of the EMICD.

the detectors inside the end calorimeters, peaks near 0, as expected. Therefore, with the addition of the EMICD, we have very good electron identification efficiencies. Work is underway to develop an H-matrix approach to electron identification in this region similar to the technique used for the liquid argon EM calorimeters. We are also studying the efficiencies for discriminating between an electron and a photon by using the information available from the scintillating fiber tracker.

The histograms in Figures 15 and 16 show the distribution of reconstructed energy in the calorimeter only, energy in the EMICD, and energy in the calorimeter + EMICD + ICD. (The central preshower is not included, since in the current version of the upgrade simulation, there are no sampling weights associated with it, and it only extends to $\eta = 1.2$.) These plots show that the energy resolution degrades somewhat at higher rapidities due to unavoidable dead material in front of the EMICD. However, except for precise mass measurements, most physics topics will benefit from the increased acceptance provided by the EMICD. In all cases the energy resolution is improved compared to the old detector with no EMICD.

In Figure 17 the energy per layer is shown. The EMICD layers are given layer numbers corresponding to the missing EM calorimeter layers. Clearly, a large fraction of the electron shower energy is deposited in the EMICD. Full incorporation of this detector into the current electron identification scheme will require more GEANT studies as well as test beam studies, in order to accurately parameterize the electron and pion shower profiles in terms of H-matrix coefficients.

Each η bin in the intermediate region is different, and the effect of the EMICD also changes with eta. In the first bin, $1.1 < |\eta| < 1.2$, three out of four EM calorimeter layers are available. The central preshower will extend to cover most of this η bin. Electrons can be identified currently in this region with poor efficiencies, the primary problem in this bin being a degradation in energy resolution. Here the EMICD serves as a 'tailcatchher', sampling the end of the electromagnetic shower with improved resolution over the present ICD. The combination of the central preshower and EMICD should completely restore electron ID with good energy resolution in

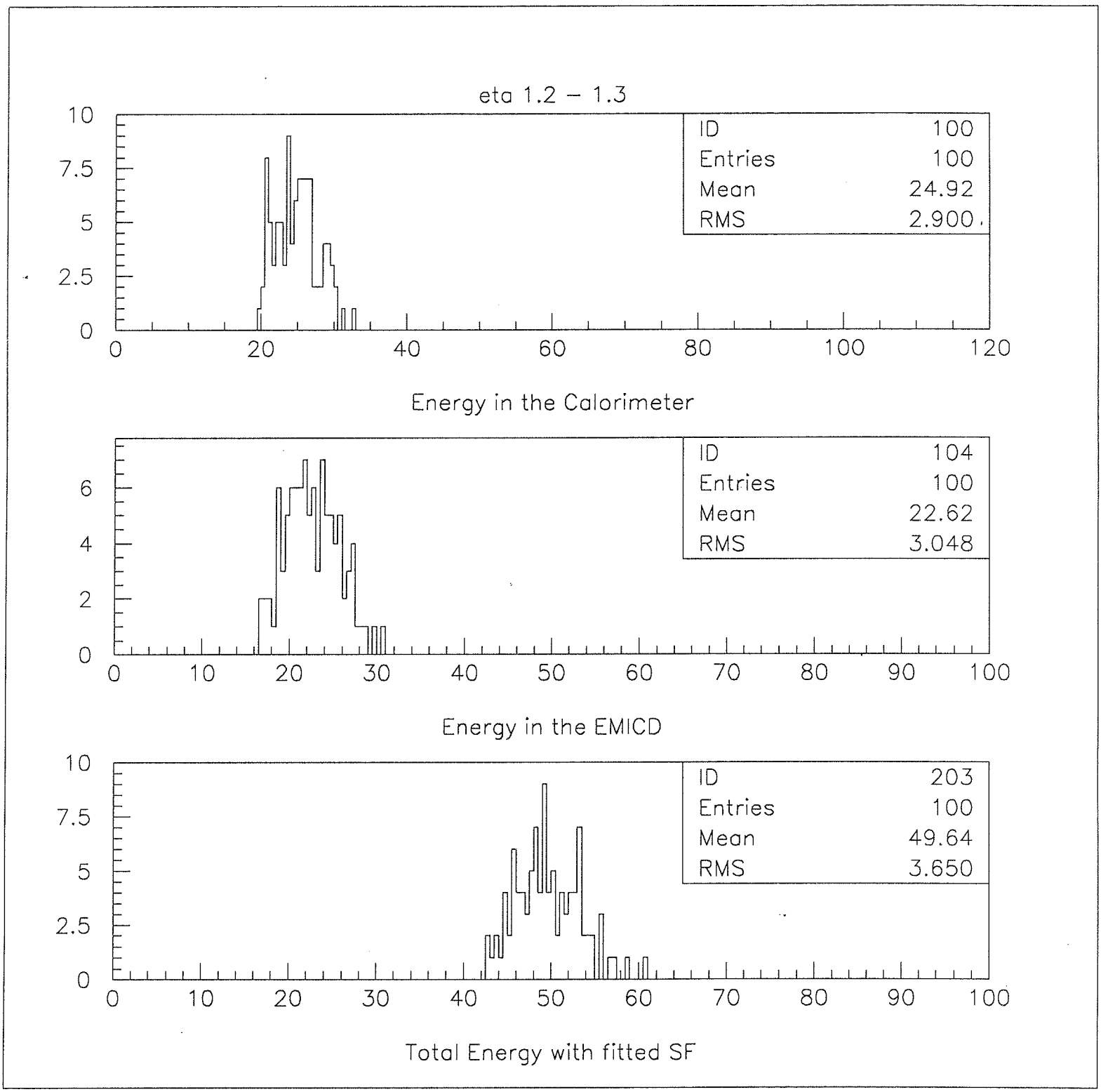

Figure 15: Results of GEANT simulations of the EMICD in $1.2 < |\eta| < 1.3$, showing energy deposition of 50 GeV electron in a) the calorimeter + ICD/MG, b) the EMICD only, and c) the calorimeter + EMICD + ICD/MG

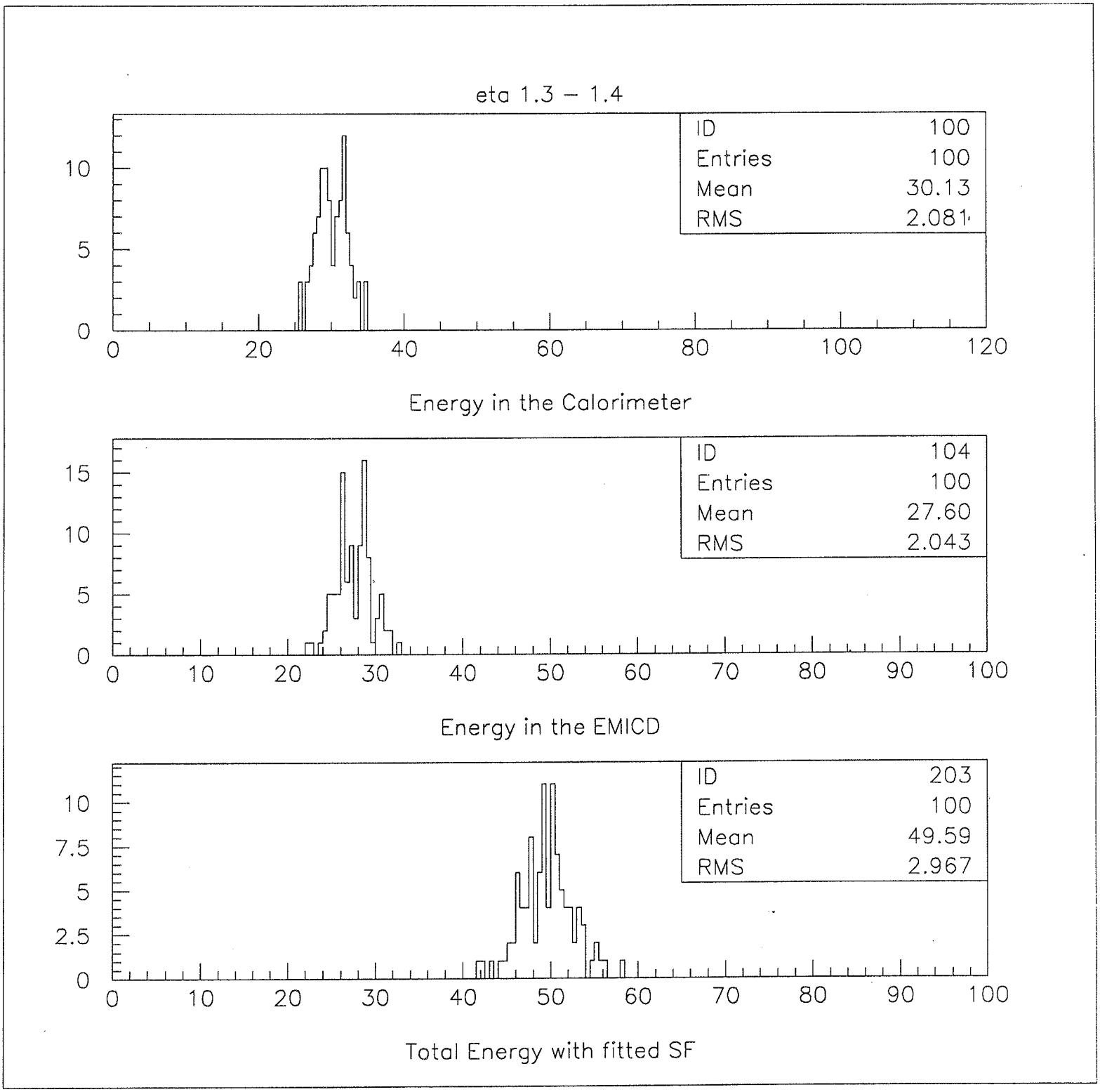

Figure 16: Results of GEANT simulations of the EMICD in $1.3 < |\eta| < 1.4$, showing energy deposition of 50 GeV electron in a) the calorimeter + ICD/MG, b) the EMICD only, and c) the calorimeter + EMICD + ICD/MG

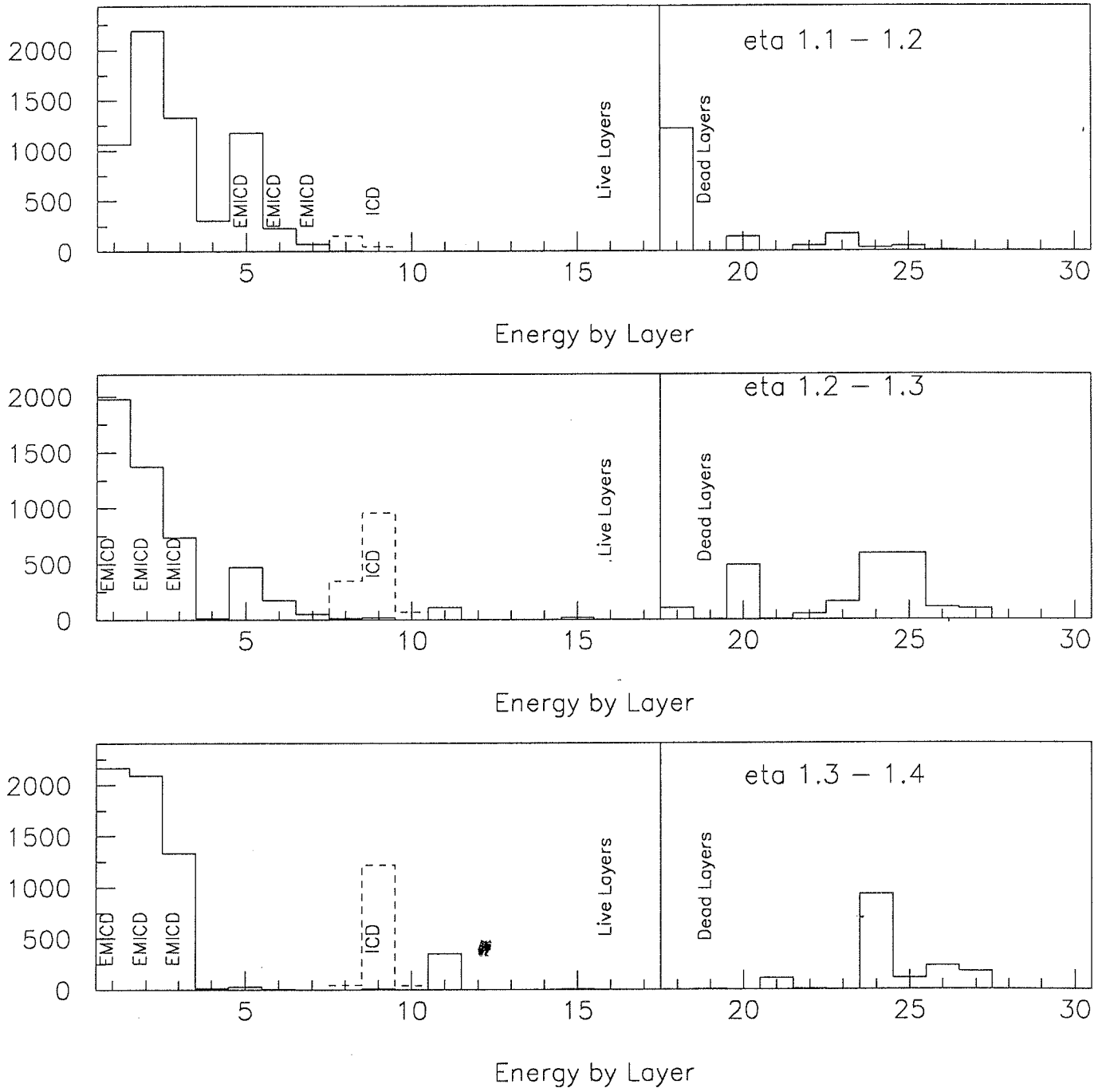

Figure 17: Longitudinal energy deposition by layer number for 50 GeV electrons. Each subplot is for a different η of the incident electron

this η bin.

In the next bin, $1.2 < |\eta| < 1.3$, there is almost no EM coverage (a small piece on EM1 covers part of the region). There will be no coverage by the central preshower in the current upgrade design. Shower maximum for the electromagnetic shower actually occurs in the EMICD. The only possiblility for electron identification in this η bin is with an EMICD plus central tracking.

In the third bin, $1.3 < |\eta| < 1.4$, there is no EM coverage (the EM3 and EM4 sections in the endcaps are not instrumented). The 'knuckle' in the central cryostat covers half of this η bin. Shower maximum for electromagnetic showers actually occur in the cryostat or EMICD. Again, the only possiblility for electron identification in this eta bin is with an EMICD plus central tracking that extends to at least $\eta = 1.4$.

3.4 Baseline Design

The proposed EMICD will consist of layers of lead and scintillating tiles, with the scintillation light carried from the tiles via wavelength- shifting (WLS) fibers. The WLS fibers are spliced to clear fibers which are then connected to photodetectors. As with the upgrade of the present ICD in η of 0.9 to 1.1, the back-up choice for readout is photomultiplier tubes, which must be placed away from the EMICD in a relatively low magnetic field region. Previous tests of ICD PMTs, with four layers of mu-metal sheilding, show that the tubes can function with little appreciable loss of gain in transverse magnetic fields of up to 200 gauss. Other possiblilties for reading out the light include mesh-dynode PMTs (which may be less susceptible to magnetic fields), PIN diodes, avalanche photodiodes, Hybrid PMTs, and VLPCs.

A starting design for the EMICD is shown in Fig 2. We propose to add three layers of Pb/Scintillator in η 1.1-1.4. We have also studied an alternate design with five layers in eta 1.1-1.2 and 1.2 - 1.3. While there is a benefit to having the increased sampling in the second η bin (where shower maximum occurs in the EMICD), the current design represents a compromise that reduces the cost of the detector while

maintaining its functionality. Clearly the same improvements in energy resolution due to increased sampling layers would also be beneficial in the problematic η bin of 1.3 - 1.4, but because of space constraints due to the readout of the central tracking elements, this is not possible. Therefore we propose three layers of Pb/Scintillator in eta 1.3-1.4, even though this is clearly the worst η bin and could use more sampling layers. The total radiation length ranges from 7.8 to 9.5, depending on η.

There are a total of 1664 Pb plates in the assembly, corresponding to slightly more than 2300 lbs per EC support structure. The readout of the tiles will be ganged together longitudinally at the PMT into towers in eta-phi. It is currently envisioned to gang the three layers into two depth readouts. This readout scheme results in a total of 768 PMT readout channels, which can be incorporated into the ADC/BLS electronics with some minor modifications. The EMICD will be positioned behind the refurbished ICD in these η bins. The total thickness of the EMICD is less that 5cm, as stipulated in the design requirements set by the upgrade management in early 1993.

The scintillator tiles will be milled with a single groove for the wavelength-shifting fiber (WLS), which will exit the tile at two points. The WLS fiber will then be spliced to clear fibers in order to transport the light to the photodetectors. The space constraints will necessiatate the use of rather thin tiles. We are currently considering 3mm and 5mm thick Bicron BC-404 tiles, with Kuraray Y11 WLS fibers. We will study ways of maximizing the light output of the tile/fiber assembly, drawing on our previous experience in developing the ICD as well as the experience of ourselves and others (CDF [14], SDC [15]) with similar tile/fiber assemblies.

For the ICD, three stages of calibration have been critical :

- Determination of the sampling fractions and linearity using protoypes at the Test Beam,
- *In situ* calibration with MIPs, as well as individual calibration of each channel with cosmic rays to determine relative gains; and

- A LASER-based *in situ* gain monitoring system.

A similar calibration scheme will be pursued for the EMICD. In addition, the upgraded DØ detector will allow E/p *in situ* calibration with electrons measured by the central tracker in the magnetic field. Similar to the original ICD, Tile/fiber assemblies will be calibrated on a cosmic-ray test stand in order to establish a MIP signature per assembly. This MIP signal must be reconstructed later in the detector; this requirement effectively sets the low-end sensitivity of our light detectors, and tends to bias the choice towards PMTs.

3.5 Conclusion

We propose a new electro-magnetic sampling detector, EMICD, to provide electron identification and measurement in the intermediate 'EM hole'. This detector will increase the acceptance for numerous physics topics. A baseline design for the EMICD is presented. GEANT studies show that this detector can identify electrons from pions with good efficiency. Further studies are underway. Prototype work being carried out for the ICD will be directly usable for the EMICD. A budget and schedule are appended at the end of this document.

4 THE FORWARD PRESHOWER DETECTOR

4.1 Motivation

With the addition of the solenoid and the central (barrel) preshower detector, DØ will enjoy improved electron and photon identification capabilities in the central region for Run II. However, there are currently no provisions to extend similar capabilities to the forward region.

The endcap liquid argon calorimeters provide excellent energy measurement and position resolution for isolated high P_T objects, as originally designed. However,

for low P_T electrons, for non-isolated electrons from b-decays, and for distinguishing photons from π^0's, the calorimeter position resolution is inadequate, primarily due to the cell size of $\eta = 0.1/0.05, \phi = 0.1$. A finely segmented forward preshower detector coupled with forward tracking upgrades could significantly improve calorimeter capabilities in these areas.

One of the major inefficiencies with electrons in the forward region arise from the high trigger rates for electromagnetic objects. Most of the triggered objects are QCD jets which are rejected in the reconstruction. Rejection of backgrounds to electrons (both low energy and high energy) can be improved with a high resolution forward preshower detector.

4.1.1 Direct Photons and PDF

Measurement of direct photon cross-section provides a sensitive technique for determining gluon structure functions. Currently, results obtained from direct photon studies in the central region are limited by large errors in the absolute cross sections. Some of these systematic errors can be reduced if the ratio of central to forward direct photon production can be measured in the same experiment. Figure 18 shows the invariant cross section for the production of photons with transverse momentum P_T =10 GeV (a) and P_T = 20 GeV (b) as a function of the η of the photon. It demonstrates the sensitivity of the cross section in the forward direction to the choice of a few different parameterizations of the gluon parton distribution function (PDF) [10]. The error bars are the statistical errors corresponding to an integrated luminosity of $1pb^{-1}$ assuming 100% detection efficiency. The gluon PDF was parameterized as

$$xG(x) = x^{-\epsilon}(1-x)^b \tag{1}$$

where the parameters ϵ and b were only allowed to vary over a range allowed by the currently available experimental data. Since the Compton diagram dominates at low P_T regions, the greatest sensitivity to the parameters is clearly at small P_T and high pseudorapidity. Therefore, it is essential to measure the direct photon cross section

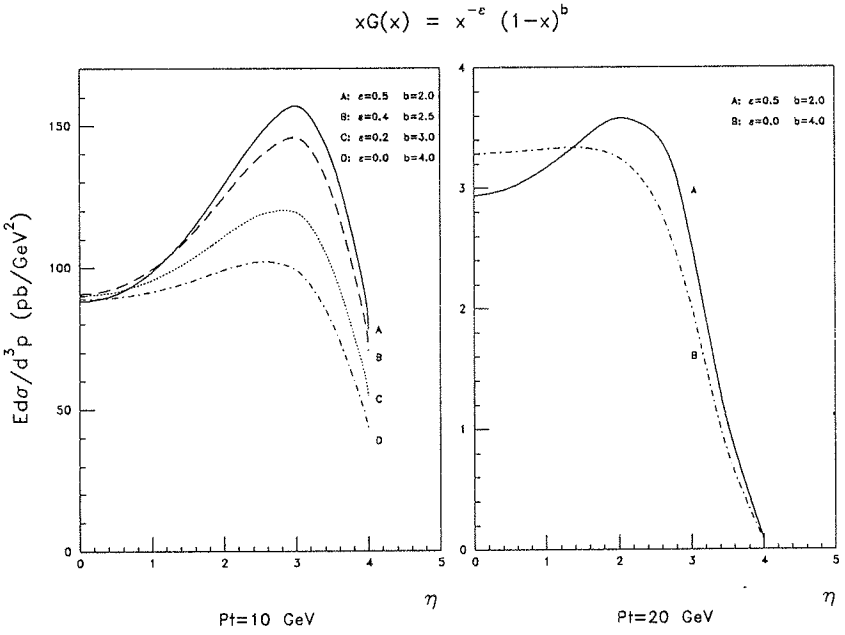

Figure 18: Invariant cross section for direct photon production as a function of photon pseudorapidity for different parameterizations of the gluon PDF for photons with (a)P_T =10 GeV/c and (b)P_T =20 GeV/c.

at the lower P_T in the forward region to understand the small x behavior of the gluon PDF.

The dominant source of background to high energy direct photons come from π^0's which are copiously generated in high P_T events. The two gammas produced in the decay of a π^0 merge into a single electromagnetic cluster and cannot be distinguished from a single isolated photon. Direct photon analysis in the current run suffers from the lack of accurate information of the photon fraction in the candidate sample. Two methods are used in DØ to estimate the photon fraction in the central pseudorapidity region. The conversion method which uses central tracking dE/dx information and the calorimeter method which uses shower shape information do not agree with each other. Therefore, the inclusive cross section measured from run Ia suffers from large systematic errors caused by the inaccurate estimation of the photon fraction. This problem gets worse for low P_T electrons because of the increasing uncertainty of photon fraction estimation at lower energies [16]. Currently, the low P_T limit used in the cross section measurement is 10 GeV.

The inclusive P_T spectrum of the photon in the forward region was reported at the APS meeting in 1994. This cross section measurement used the conversion method in the forward drift chambers (FDC) to estimate the photon fraction. Figure 19, shows the MIP distribution of the candidates for $10 < P_T < 22$ GeV photons [17]. One can see that at low P_Ts, it is difficult to distinguish the photon fraction, thereby causing large systematic errors. As we discussed above, the most sensitive determination of the gluon PDF is obtained at photon P_T =10 GeV in the forward ($\eta \approx 2.5$) region. However, with the current detector configuration is almost impossible to achieve an accurate measurement of the cross section.

In order to measure the forward cross section more accurately, it is not necessary to unambiguously identify every direct photon - it is only necessary to identify enough π^0 decays to accurately predict the magnitude of the π^0 background. We studied the prospect of separating direct photons from merged $\pi^0 \rightarrow \gamma\gamma$ decays to determine the spatial resolution required to extend the direct photon analysis to appreciably

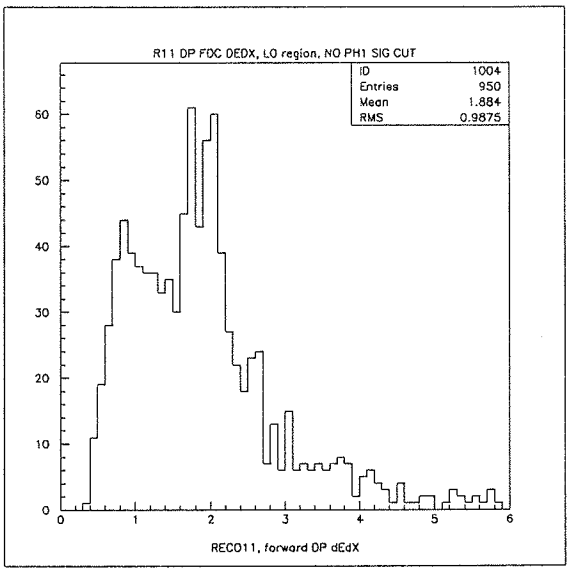

Figure 19: MIP distribution of electron candidates in FDC for $10 < P_T < 22$ GeV.

higher η than has been done with the present detector. It should be noted that, since this study was performed at the ISAJET level, shower and energy smearing were neglected; and we have assumed that if the forward tracking is good enough to identify photons in the FPS, then the mere observation of two showers is sufficient to veto π^0 candidates. Figure 20 shows the probability of $\pi^0 \rightarrow \gamma\gamma$ merging as a function of the FPS spatial resolution in four different bins of η, (a) all η, (b) $1.6 < \eta < 1.8$, (c) $2.0 < \eta < 2.2$, (d) $2.4 < \eta < 2.6$, and (e) $2.8 < \eta < 3.0$ for three different regions of E_T^γ (triangles are for $20 < E_T^\gamma < 25$GeV; squares are for $15 < E_T^\gamma < 20$GeV; and circles are for $10 < E_T^\gamma < 15$GeV). This figure indicates that a FPS with two-shower separation resolution of 4mm should be able to veto merged π^0's at the 50% level for E_T as high as 25 GeV out to $\eta \sim 2.0$; E_T as high as 20 GeV out to $\eta \sim 2.4$; and E_T as high as 15 GeV out to $\eta \sim 2.8$.

4.1.2 Top Quark & b Physics

The improved position resolution provided by a preshower detector could also improve the identification of non-isolated electrons. For example, electrons from the semi-

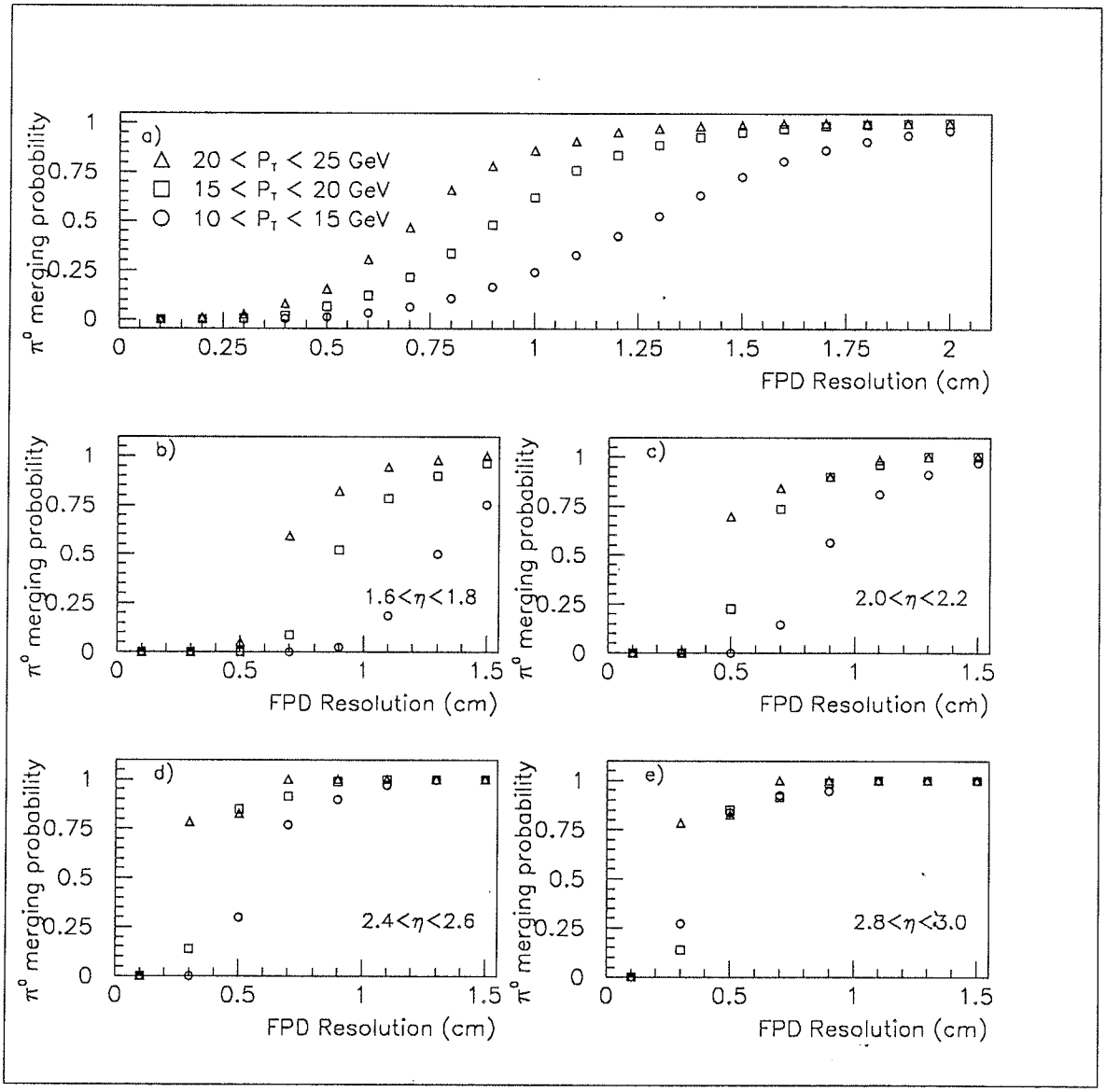

Figure 20: The merging probability that two γs from a π^0 decay will form a single cluster as a function of detector resolution in different η regions.

leptonic decay of b-quarks are produced near jets. Tagging such non-isolated soft leptons can significantly increase b-physics capabilities.

Top quarks are produced in pairs at the Tevatron, then immediately decay into W's and b quarks resulting in many different signatures for the final state. Identification of the signal from top quark decays is difficult due to the large backgrounds from the copious production of W + multijet events. The background rate is substantially decreased if the associated b quark can be identified. Therefore, identification of a soft electron in W multijet events can greatly enhance the top signal. About 20% of all top decays have a jet with a soft electron.

The parton distribution functions of charm and bottom quarks are not directly measured from deep inelastic experiments and are not well known. Charm and bottom quark jets balancing a direct photon which decay semileptonically will yield a soft lepton associated with the jet. Measurement of the forward cross section of these process can provide a direct measurement of the charm and bottom contents of the sea quarks. The semileptonic branching ratio of inclusive b decays is as large as 11%[5], leading to high event rates. The forward preshower can help this measurement in two ways: by improving the identification of direct photons and by improving the identification of soft leptons.

An ISAJET study of b quark production in the forward preshower region shows that most b jets containing a soft lepton do not have any other particles within a 1 cm cone in the FPD region out to $\eta \sim 3.0$. The calorimeter segmentation is too large to separate these soft electron showers from the accompanying jet. However, a FPD with 2-4 mm segmentation can identify the electron cluster and therefore tag b jets. In this study we assumed a uniform solenoidal magnetic field of 2T, neglected photon conversions, did not decay π^0's, and required that $E_T^e > 5$GeV to insure tagged electrons would deposit observable energy in the electromagnetic calorimetry. Figure 21 presents the electron tagging efficiency as a function of the FPS resolution in several different bins of η. This plot shows that, even for FPS resolution of 1 cm, electrons can be tagged within jets out to the highest η proposed. In Figure 22 we

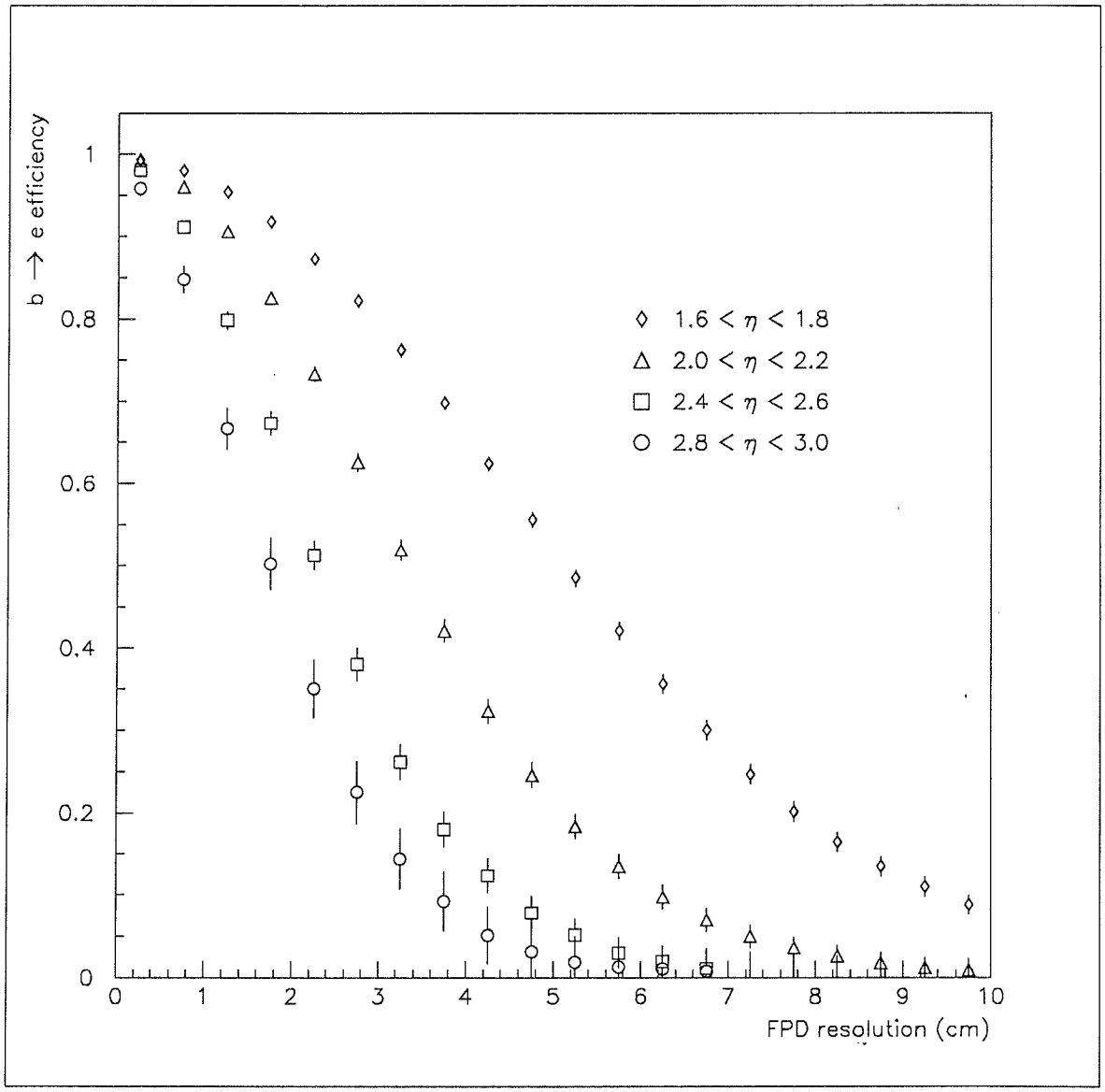

Figure 21: Electron tagging efficiency as a function of resolution in the FPD for b decays

show the average number of inclusive particles as a function of cone size centered on the direction of the electron from the b decay. This plot demonstrates why the 0.1 radian cell size in the EC is insufficient for tagging b electrons.

4.1.3 W/Z Physics

It is important to measure the cross sections for the production of multiple jets produced in association with W bosons because the perturbative QCD predictions for these processes are calculated only in leading order (LO). $W+$ multijet events are the biggest source of background for the top search in lepton+jets channel. Therefore, without an independent measurement of the production mechanism of $W+$ multijet processes for all jet multiplicities, the background estimates to the top quark production will suffer from inherent systematic errors.

Approximately 30% of the electrons from W decay are in pseudorapidity $\mid \eta \mid > 1.5$. However, the background rate from QCD fake electrons which largely consists of an energetic π^0 associated with a low energy charged track is much higher in the forward region compared to the central region. The forward preshower detector can help reduce this background.

At the center of mass energy of 1.8 TeV, W bosons are produced dominantly from valence-valence or valence-sea quark annihilation processes. The center of mass angular distributions of the leptons from the W decay can provide information[11][18] on the parton momentum distributions at low Bjorken x as well as at high momentum transfers. The W^+ boson couples u quark with d-bar quark and the W^- couples u-bar with d quark. Thus the W^+ will be produced primarily by the u-quark from the proton and d-bar quark from the antiproton. Because valence u quarks from the proton carry more momentum on the average than the valence d quarks, the W^+ will tend to be boosted along the direction of the proton and the W^- will be boosted along the antiproton direction. Therefore, a measurement of the asymmetry in rapidity distributions of the W bosons provides valence u and d quark parton distribution functions. However, due to the neutrino in the leptonic decay of the W,

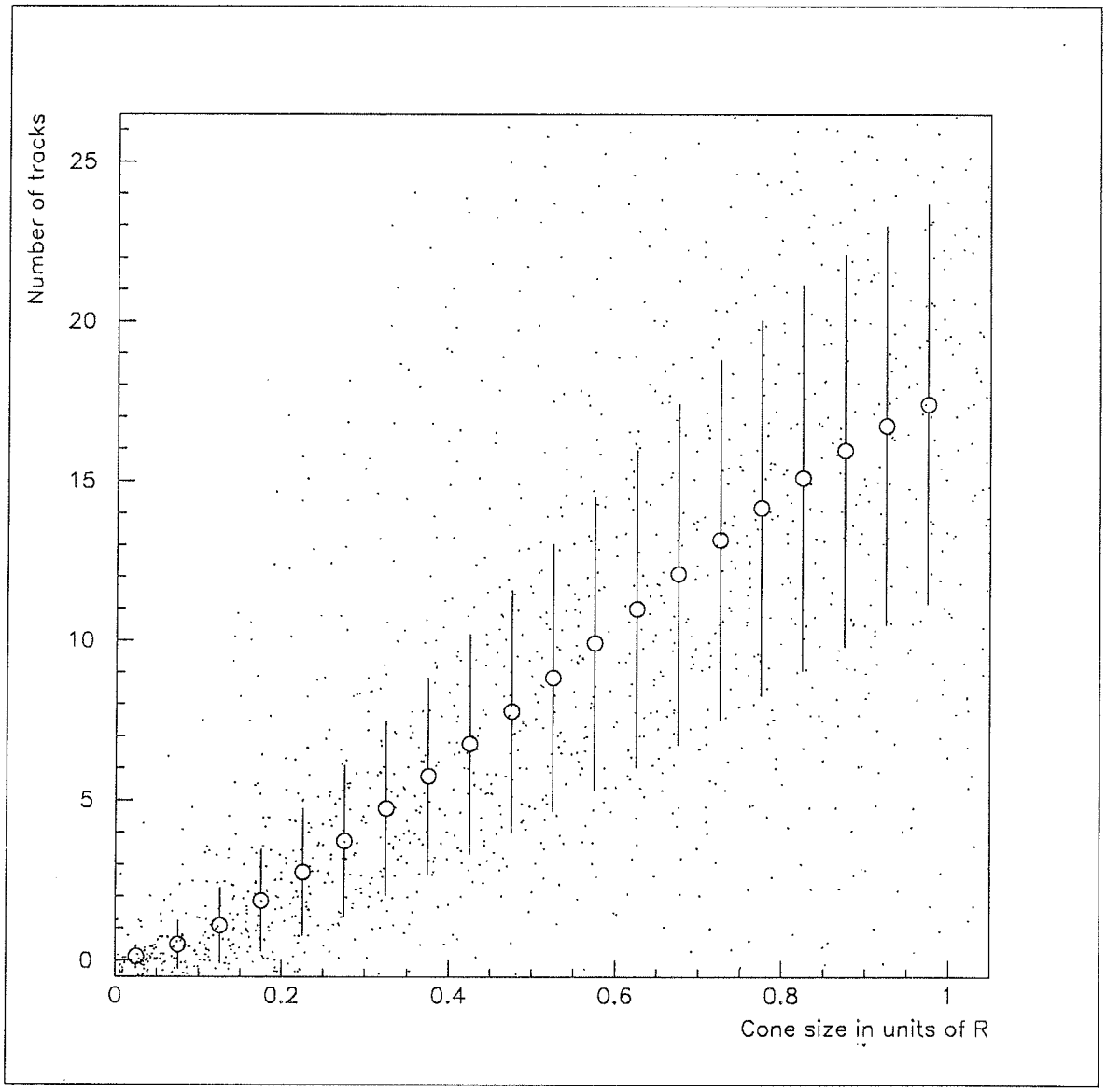

Figure 22: The average number of tracks within different cone sizes centered on the electron from b decays

the longitudinal momentum of the W always includes a two fold ambiguity. To avoid the ambiguity, the angular distribution of the charged leptons from the W decay is traditionally used for this asymmetry measurement. The forward preshower detector can help with the identification of the charged leptons in this measurement. It is important to mention here that for this measurement and for most other physics topics mentioned here, it is crucial to have good forward tracking in the upgraded DØ detector. For example, the charge of the electron in the W decay can only be obtained from the tracking detector.

A precise measurement of the $WW\gamma$ coupling can be very useful for probing new physics beyond the standard model[19]. This coupling can be studied at DØ through $W\gamma$ production. Currently, the measurement is statistics limited. With the help of the FPD, the event rate can be increased greatly. If the measurement is restricted to $|\eta| < 1.0$, only 27% of the events occur within the fiducial region. 31% of the photons from this process occur in the region $1.4 < |\eta| < 2.5$, which could be identified with the FPD. The FPD can also help with the identification of an additional 21% of the events where the electron is in this region[20].

4.1.4 New Particle searches

Test beam studies have shown that the DØ calorimeter system has good linearity and energy resolution at low energies. However, poor background rejection for low energy electrons limit their use in physics analyses. Due to the coarse segmentation of the calorimeter cells, the overlap of π^0's with low energy charged pions can fake low energy electrons. The FPD can help with electron identification by improving the position resolution and by providing better triggering.

Several SUSY search channels include final states with multiple electrons, some with rather low p_T . As examples of these searches, we have considered decays of charginu-neatralino pairs into trileptonic final states and decays of light stop squarks.

The search for pair production of the lightest chargino ($\tilde{W}_1$) and next to lightest

neutralino ($\tilde{Z}_2$) SUSY states is a complementary search channel to squark/gluino searches. The most promising final state is the trileptonic configuration, with three leptons (two of them an oppositely charged pair) plus missing E_T . This channel can probe from $M_{\tilde{W}_1} = 45$ GeV (the LEP I limit) to 200 GeV (where other decay modes begin to dominate, destroying the trilepton channel). For the low end of the mass spectrum, the p_T of the lowest p_T electron can be rather low, pushing the limits of DØ 's electron identification capabilites.

We show below in Table 5 the increase in acceptance for this search for various integrated fiducial regions. Trigger conditions are approximated by considering events with two electrons of p_T greater than 10 GeV, or one electron of p_T greater 20 GeV. The percentage of accepted events is given out of the total number meeting the trigger criteria.

Fiducial Boundary in η	Events Accepted *eee* channel 3 e's, $p_T \geq 5$ GeV	Events Accepted *eee* channel 1 e, $p_T \geq 20$ GeV + 2 e's, $p_T \geq 5$ GeV	Events Accepted $e\mu\mu$ channel ${p_T}^e > 5$ GeV
-1.0 – 1.0	25.7%	44.1%	56.7%
-1.4 – 1.4	46.3%	51.1%	74.0%
-2.5 – 2.5	91.1%	94.1%	97.5%
-4.0 – 4.0	100.0%	100.0%	100.0%

Table 5: Increase in acceptance for $\tilde{W}_1$ / $\tilde{Z}_2$ searches as a function of the η coverage of the upgraded detector

Large mass splitting may exist betweeen the right- and left-handed states of the SUSY partner particle to the top quark (and to a smaller extent, to the bottom squark and tau slepton). There is the possibility that this mass splitting may lead to a stop that is much less massive than the top.

The search for a light stop is being pursued in two channels : jets + $\not\!\!E_T$, and dilepton + jets + $\not\!\!E_T$. The jets + $\not\!\!E_T$ search has many of the same features as the "traditional" squark/gluino $\not\!\!E_T$ search [6].

Alternatively one can look for $\tilde{t} \rightarrow b\tilde{W}_1, \tilde{W}_1 \rightarrow e\nu\tilde{Z}_1$ or $\mu\nu\tilde{Z}_1$. Both stops are required to decay to a lepton due to inefficencies in tagging b jets. The total cross section for stop production is about 1/10 that of top production at the same stop/top mass. For a 70 GeV stop, the cross-section is roughly 20 pb. Approximately 5% of stop decays to $b\tilde{W}_1$ will be to ee, $e\mu$, and $\mu\mu$. Thus $\sigma * BR \approx 1pb$ at 1.8 TeV. If $\tilde{t} \rightarrow b\tilde{W}_1$ is kinematically allowed, it will completely dominate the cross section, otherwise $\tilde{t} \rightarrow c\tilde{Z}_1$ will be the only mode. Table 6 gives the frequency that at least one electron from $\tilde{t}\bar{\tilde{t}} \rightarrow ee$ or emu is in a given eta region.

	ee channel		$e\mu$ channel	
η Bin	70 GeV $\tilde{t}$	90 GeV $\tilde{t}$	70 GeV $\tilde{t}$	90 GeV $\tilde{t}$
0.0 – 1.0	83%	89%	64%	68%
1.0 – 1.2	19%	15%	8%	10%
1.2 – 1.4	15%	11%	7%	7%
1.4 – 2.5	31%	28%	17%	12%
2.5 – 3.4	5%	4%	3%	3%
1.0 – 1.4	32%	26%	15%	17%
1.4 – 3.0	34%	30%	19%	13%
Both in 0.0 – 1.0	40%	47%	–	–

Table 6: Increase in acceptance for Stop searches as a function of the η coverage of the upgraded detector

Even though the FPD is not essential for some of the searches mentioned above, (forward tracking IS essential) since they involve high P_T electrons, the FPD can help with triggering and provide a cleaner sample of electrons.

4.1.5 Low Energy Electron Response

The current DØ electron identification algorithms were tuned to optimize identification effeciency for electrons above trigger thresholds. In Figure 23, the identification efficiency for low p_T electrons is shown. This plot is based on single electrons studies using the plate-level D0Geant detector simulation, with noise added. For low energy

electrons, identification can be relatively poor, dropping below 50% for electrons of 5 to 10 GeV P_t, with H-matrix and isolation cuts. For the low p_T electrons, the FPD can play a significant role in electron identification and background rejection in the forward region.

4.2 FPD Design

We considered three different designs for the FPD. All three designs are based on scintillator sampling. In all three cases, we propose to use clear fibers to transport the light from the scintillator to Visible Light Photon Counters (VLPC) which are already being developed by DØ for the central region upgrades.

A scintillator based detector was chosen as our baseline for the following reasons:

- Low cost.
- Large dynamic range: better than 10^4 (limited only by the VLPC dynamic range). This provides the ability to have good energy resolution for both minimum ionizing particles as well as electron showers.
- Good segmentation capabilities: down to 4 mm in one dimension with a single layer. Factor of 2 improvement for each additional layer.

We propose to mount the FPDs on each end cryostat. They will extend from 1.8 to 3.0 in η. The outer radius is at 51 cm ($\eta = 1.8$) to provide enough clearance for the proposed ICD$^+$ detector which has to extend far enough to sample showers originating in the solenoid cryostat. The inner radius at 15 cm is limited by the minimum segmentation possible with scintillator strip detectors. The high occupancy (even at low luminosities) beyond 15 cm is another limiting factor. However, the detector can be extended closer to the beam pipe by building additional overlapping layers if Monte Carlo studies prove the very forward regions to be usable.

All three designs include a pre-radiator layer as the first layer seen by particles

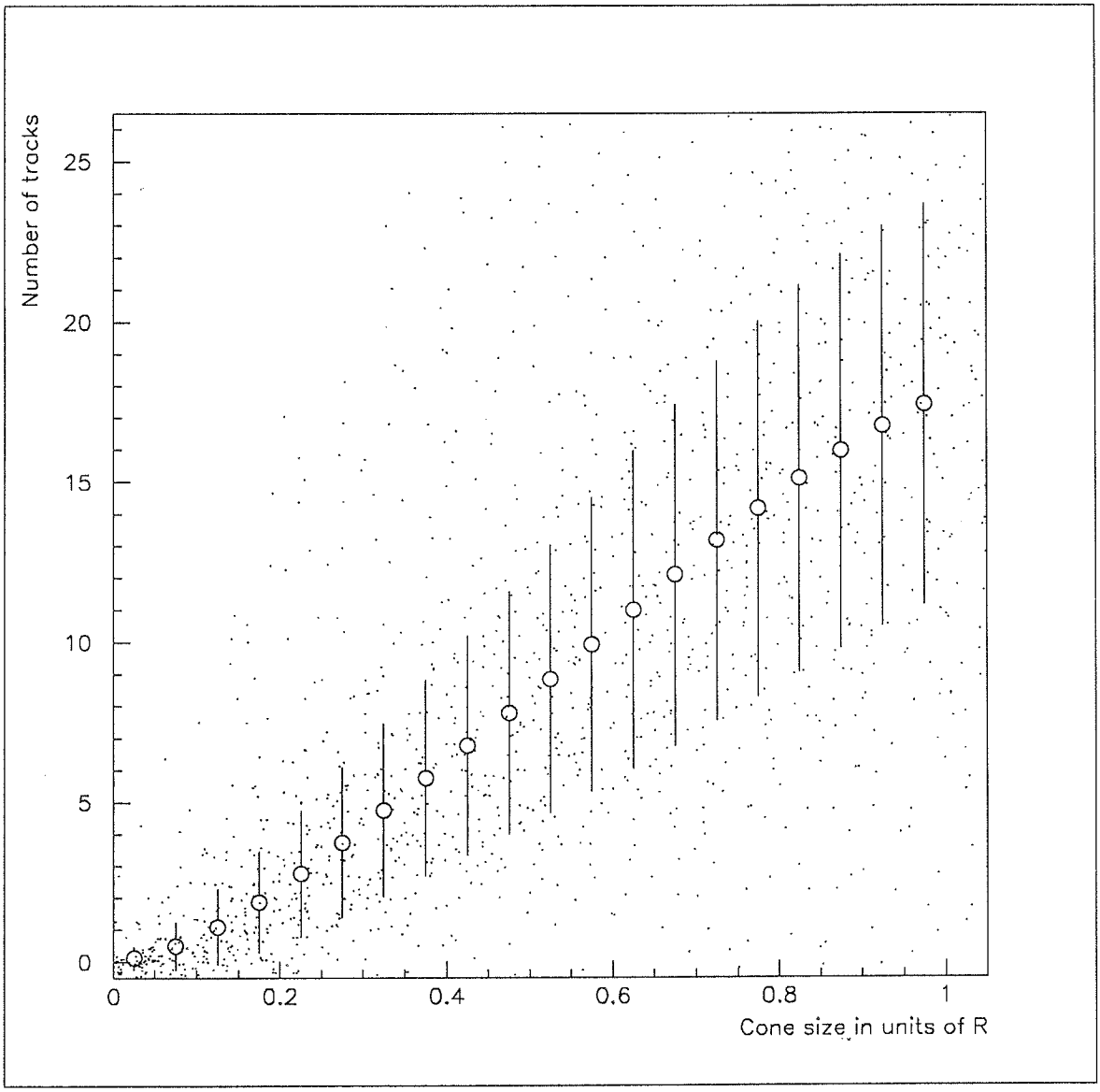

Figure 23: Electron identification efficiency, using standard H-matrix and isolation cuts. Based on plate-level D0Geant with NOISY.

coming from the interaction point. The next layer will be the lead absorber, which is followed by a finely segmented preshower sampling detector (consisting of 2 to 3 layers). We assume 5 mm thick scintillator for all layers. A blow up of the FPD region is shown in Figure 24.

4.2.1 Pre-radiator Layer

The pre-radiator layer will have coarse segmentation to match the 2x2 trigger towers in the liquid argon (LAr) calorimeters. The pre-radiator layer may also be used to monitor the live luminosity in a way similar to the current LØ detector. The total number of channels for this layer will be 384 including both sides. A schematic of the pre-radiator layer is shown in Figure 25.

Direct photon triggers at Level 1 can be generated by using the minimum ionizing signal from the pre-radiator layer as a veto for EM triggers from the calorimeter. Such direct photon triggers will have very low background rates for low P_T photons while maintaining good efficiencies.

The average shower energy of an electron after passing through a preradiator of 2 radiation lengths is about 40 times that of a minimum ionizing charged hadron. Setting a trigger threshold to the energy equivalent of 3-5 minimum ionizing particles in the post-radiator layers can provide excellent background rejection while retaining most of the real electrons. Further discrimination can be obtained with a trigger which compares shower size before and after the lead pre- radiator.

4.2.2 Lead Absorber

We have done preliminary studies of the optimal thickness for the lead. From EGS studies of electron showers, a two radiation length absorber appears to be the best choice. Using less absorber material will reduce the preshower efficiency. Adding more absorber material will degrade the energy resolution of the end calorimeters as

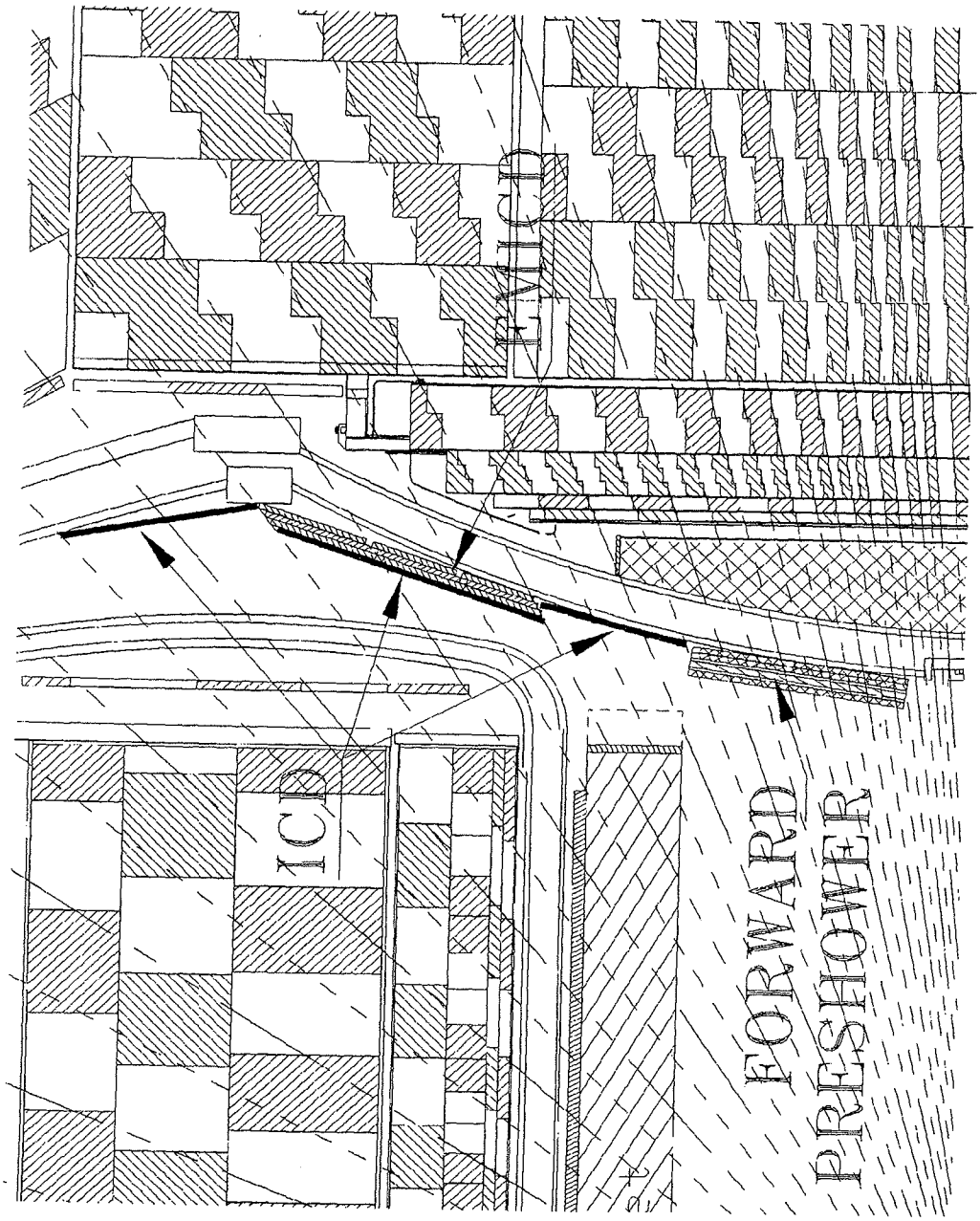

Figure 24: Expanded view of the FPD region

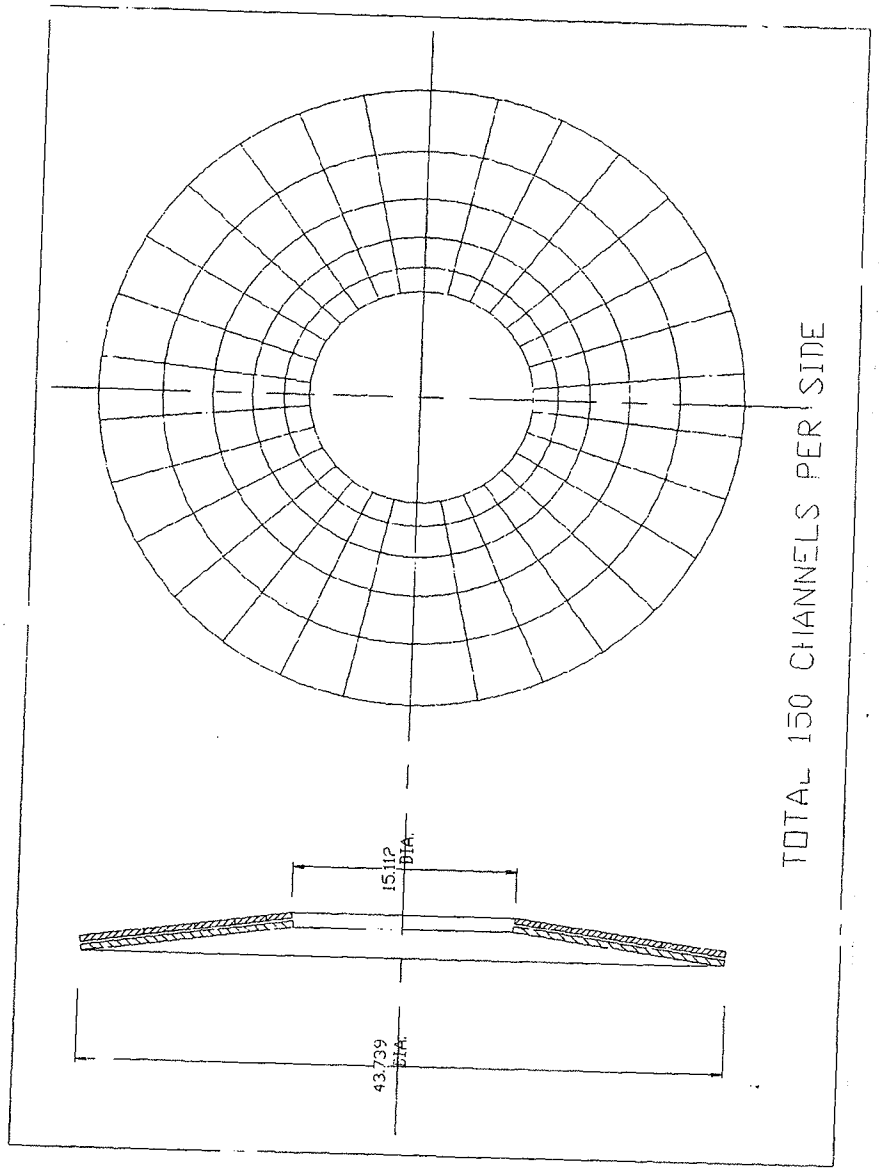

Figure 25: Pre-radiator Layer of the FPD

	0.0 χ_0	0.5 χ_0	1.0 χ_0	2.0 χ_0
50% Energy Contained	1.4 mm	2 mm	3 mm	6 mm
90% Energy Contained	14 mm	20 mm	24 mm	36 mm

Table 7: Transverse size of 50 GeV electron showers vs. upstream material

well as degrade the position resolution of the FPD by broadening the transverse size of showers.

It is crucial to keep the amount of upstream material as low as practically possible to get the best performance from the FPD. Electron showers may spread rapidly in transverse size when absorber material is placed far upstream of the FPD, thereby reducing the efficiency for electron and photon identification. We have done an EGS study with various amounts of material placed 30 cm upstream. The spread in the transverse size of electron showers after various amounts of upstream material is shown in Table 7.

4.2.3 Preshower Sampling Layer

The lead absorber is immediately followed by two to three layers of finely segmented preshower sampling. Design I for the preshower sampling layer is shown in Figure 26. This is our optimized preferred solution for the FPD. We will also briefly describe Designs II & III for comparison. These designs are less favored, for reasons which will be discussed below.

Design I consists of three layers of scintillators which provide r and ϕ information for incident particles. There is one layer of r strips which provide information on the radial position of particles with respect to the beam pipe. Two overlapping ϕ layers, identical in design but offset by half the strip width, will provide the azimuthal position of the particles. Each layer is put together from 16 pie shaped mini-wedges. The r or ϕ strips within each mini-wedge are separated by isolation grooves machined into the scintillator. Details of the strip structure is shown in Figure 27.

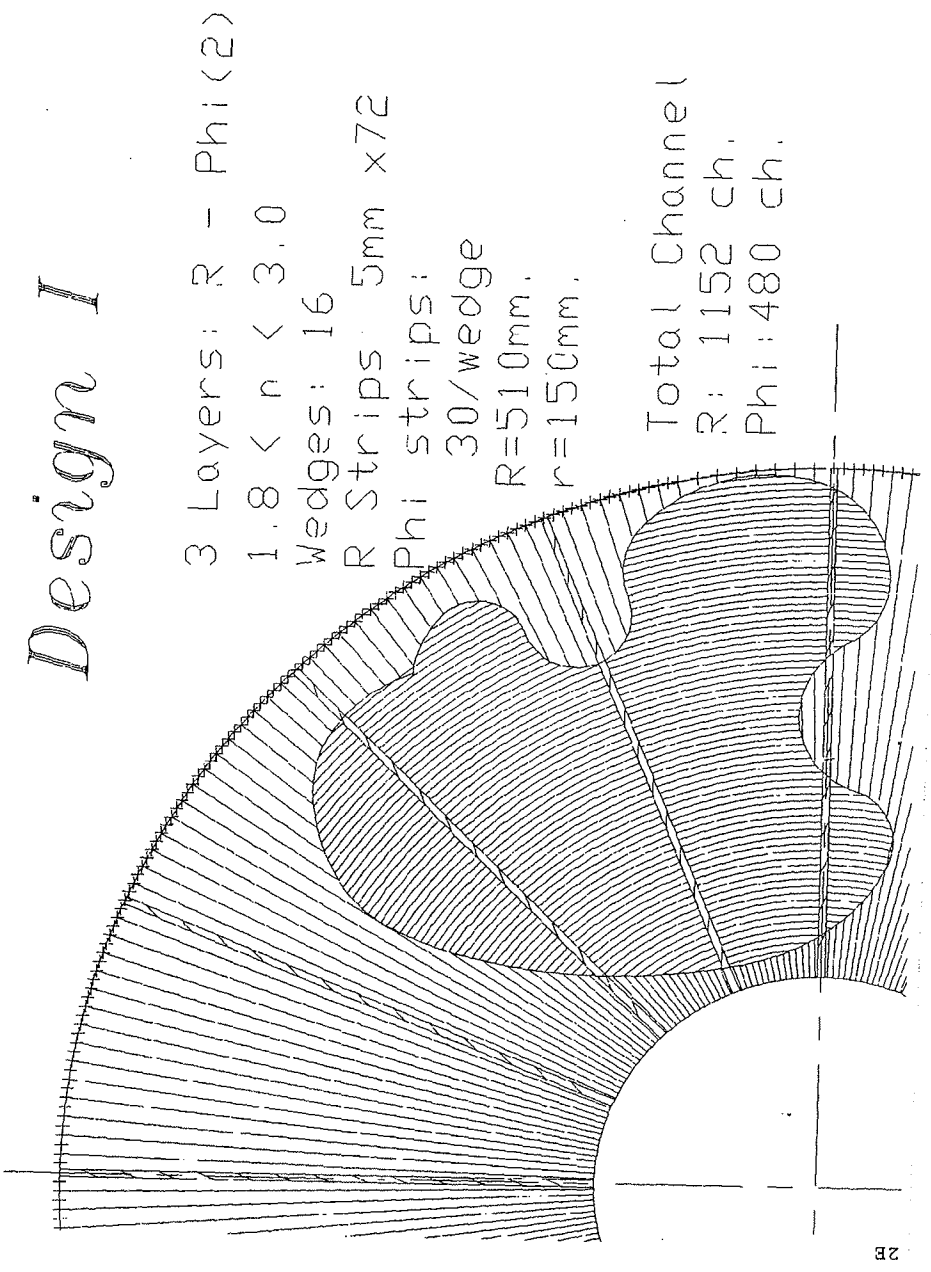

Figure 26: FPD Design I

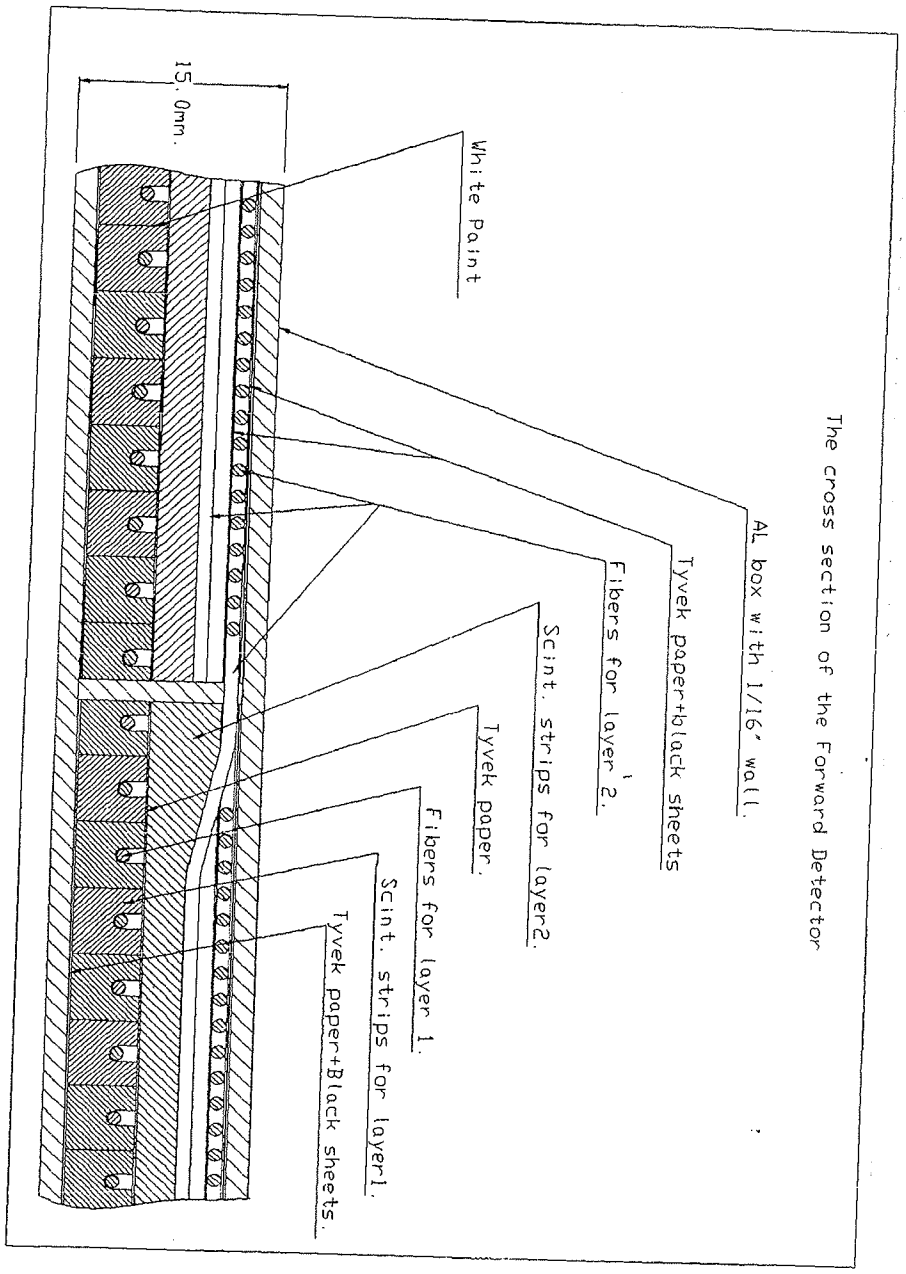

Figure 27: Details of scintillator strips in the forward preshower detector.

The r mini-wedges contain 72 annular strips. Each strip is 5 mm wide containing one wave-length shifting (WLS) fiber placed down the middle of the strip. The WLS fiber rises up from the tile near the edge and is coupled to a clear fiber which transports the light to the VLPC's. These strips provide η information. However, since all the strips have the same width, they are not constant in $\delta\eta$. Overall, this design provides a factor of 72/13 more segmentation in η than the LAr calorimeter.

There are 30 ϕ strips in each mini-wedge, for a total of 480 strips spanning 2π in each FPD. The width of the strips at the outer radius is 6.7 mm. At the inner edge it is 3.9 mm. The second ϕ layer is rotated by half the width of the strips plus the width of the isolation groove. Therefore, the two-track resolution in ϕ will be less than 2 mm at the inner edge of the detector. The average position resolution will be $2\text{mm}/\sqrt{12} = 0.58$ mm. Since the transverse shower size for 70% energy containment from 50 GeV electrons is about 2-3 mm (from EGS), the position resolution will be more than adequate for electron and photon identification. It will allow the full range of direct photon studies and b jet tagging mentioned above.

The ϕ strips provide a very high degree of segmentation compared to the calorimeter. There will be 960 total ϕ strips per side, compared to the 64 ϕ subdivisions (128 at shower maximum) in the calorimeter. A side view of the FPD as implemented in GEANT is shown in Figure 28.

We have also considered two other designs for the FPD. One design uses scintillator 'pads'. Due to the difficult design for the light readout, and to minimize channel costs, the pad design has much poorer position resolution than the Design I described above. However, in high occupancy environments, clusters are easier to reconstruct from pads. There are no ghost hits.

Our third design uses $u \times v$ geometry for the strips. Detector construction is simplified in this design. However, matching clusters in the preshower with objects in the calorimeter become complicated due to the difference in segmentation.

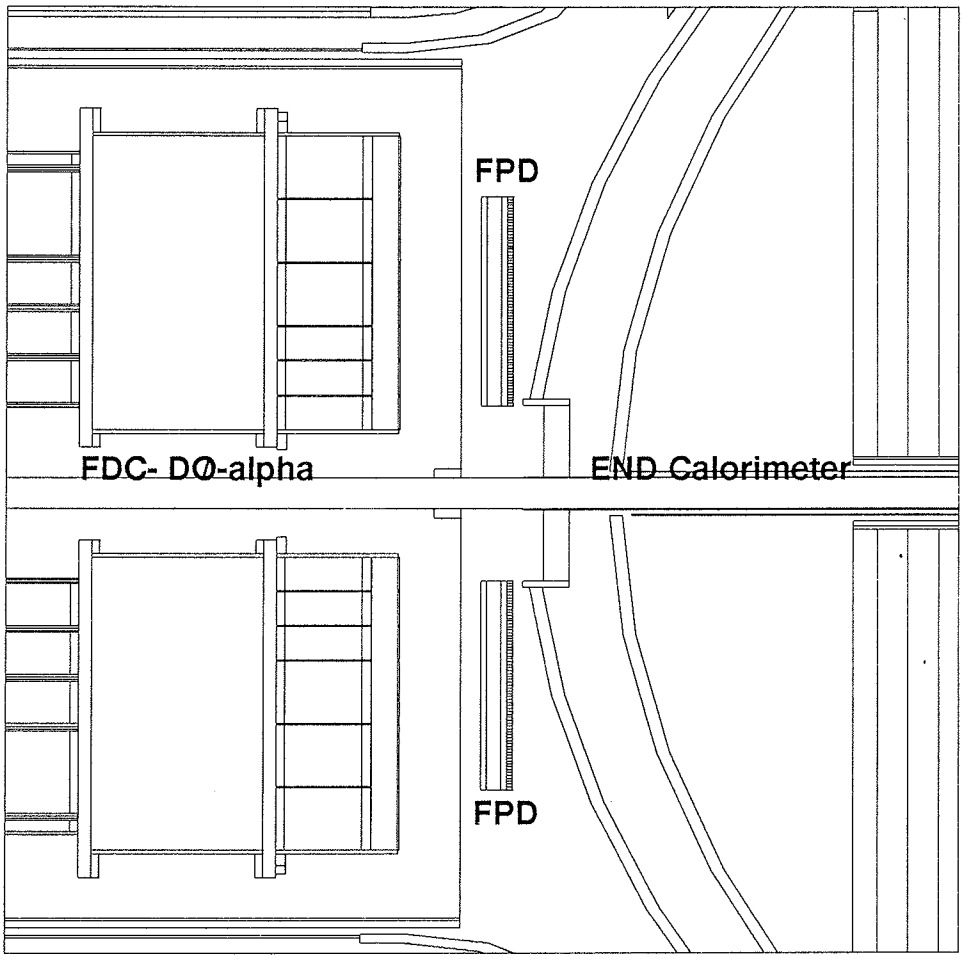

Figure 28: The FPD as implemented in D0GEANT.

4.2.4 Segmentation

The average occupancy for the FPD strips is shown in Figure 29 from an ISAJET study of two jet events. For parton jets generated between 40 GeV and 80 GeV p_T, we find 0.06 particles per ϕ strip per event in the FPD. A mini-wedge, which contains 30 strips, will have an average occupancy of 1.8 particles per event per layer. In the r strips, we find 0.03 particles per strip per event. Since there are 72 such strips in each mini-wedge, the total occupancy will be 2.1 particles. Therefore, on average, there will be ghost hits (two-fold ambiguities) for each track in every event. These ambiguities can be easily resolved by matching clusters with the calorimeter during off-line reconstruction. Ghost hits will not cause trigger problems since the tower thresholds will be set much higher than average minimum ionizing energy deposition.

4.2.5 Detector performance - GEANT Studies

In order to determine the optimal segmentation and to study the effect of the FPD on the current DØ detector, we have performed a Monte Carlo study implementing the above geometry of the FPD in DØGEANT. In this study, the FPD was integrated with the existing DØα system. We implemented a geometry which includes a two radiation length lead absorber sandwiched between two 0.5 cm thick plastic scintillator plates. The FPD was located vertically in front of the EC cryostat 1.41 m away from the nominal interaction point. Two independent studies were performed. To determine the necessary segmentation of the detector, electrons, photons, and π^0s with 10 and 50 GeV of energy were sent into the system at the pseudorapidity of 2.35. The total number of particles was 300 in each case. To study the effect of the FPD on the EM energy resolution of the ECEM, 1000 electrons with 50 GeV energy at $\eta = 2.35$ were sent into the system with and without the FPD in place. The results are described below.

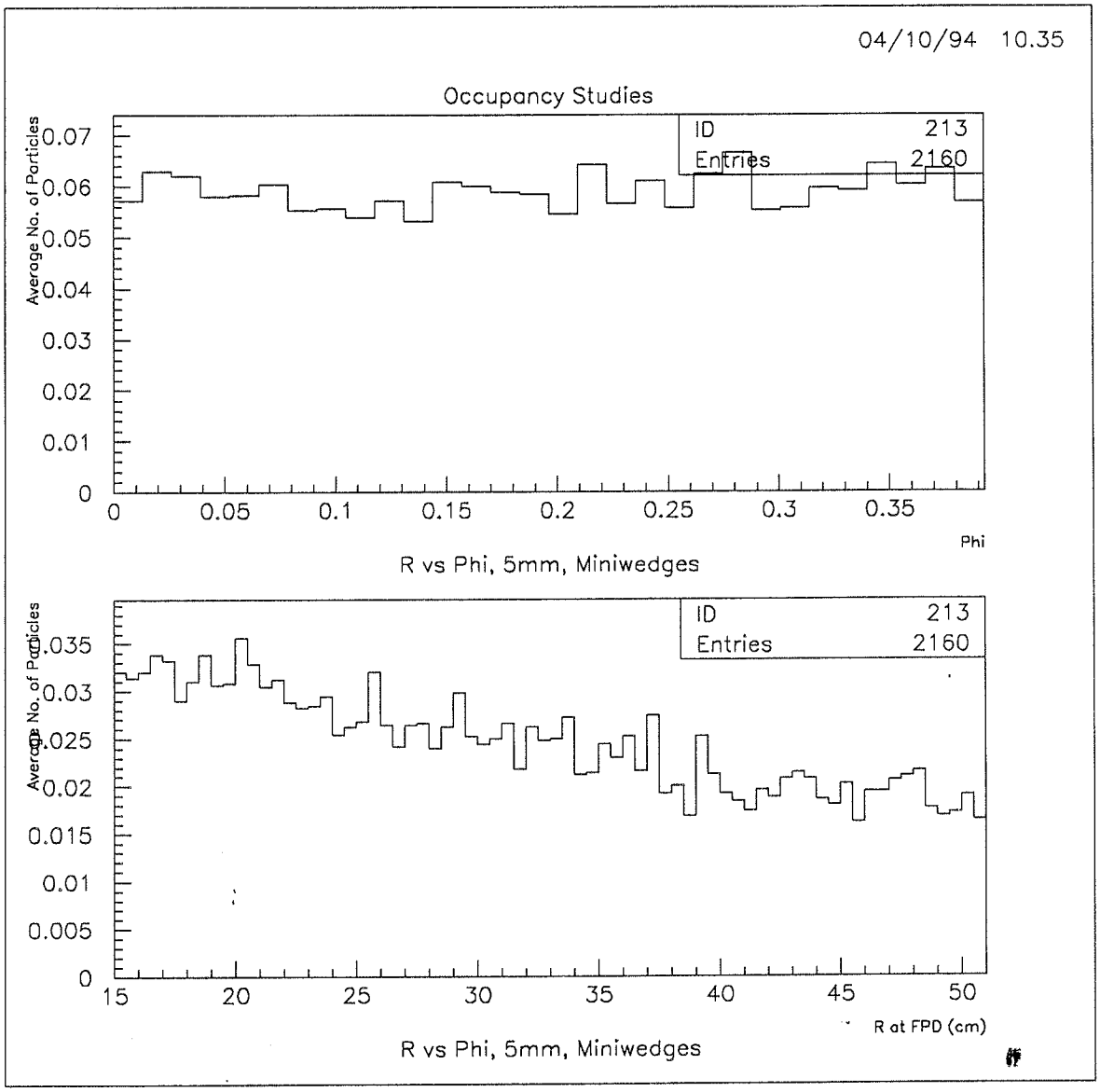

Figure 29: Average occupancy in one mini-wedge of the FPD for Design I.

4.2.6 EM shower shape in the FPD

The primary goal of the FPD is to improve electron and photon identification. In order to achieve this goal, it is important to understand the shapes of showers for various particles, especially the difference in shape between single photons or electrons and multiple photons from π^0s or other neutral hadrons. For this study, we used electrons, photons, and π^0s with energies of 10 and 50 GeV. Single particles were sent into the detector from the nominal interaction point with $\eta = 2.35$. The particles were allowed to interact within the CD volume.

The amount of material before the FPD in this setup is likely more than would found in the upgraded D$\emptyset\beta$ system with either silicon H-disks or MSGC's. We expect that the result will be approximately the same when the FPD is integrated into the upgrade simulation package, along with an agreed upon forward tracking design.

The results of the hits were recorded as the particles proceed through the FPD. Figure 30 shows the energy weighted lateral distribution of hits from secondary shower particles in the third layer (scintillator) of the FPD for 10 GeV particles. From top to bottom, the plots show the distribution of hits for electrons, photons, and π^0s. The distributions were fit to a gaussian function in order to give a representative width to each distribution. Approximately 2σ of the shower includes 90% of the total energy. As expected, the shower shapes of photons and electrons are indistinguishable. The shower shape of the π^0s are much broader then that of photons at 10 GeV.

Figure 31 shows the lateral shower shape for 50 GeV particles. As expected these plots show much narrower shower shape compared to that of 10 GeV particles. However it is still possible to distinguish the showers generated by π^0s from those generated by single photons as long as the lateral position resolution of the FPD is better than 2 mm. It is important to distinguish π^0s with 50 GeV energy, because at this pseudorapidity, $\eta = 2.35$, 50 GeV of energy corresponds to approximately 10 GeV in E_T. As mentioned in section 4.1, the direct photon cross section as a function of photon η for 10 GeV E_T is a key to better discrimination of different PDF

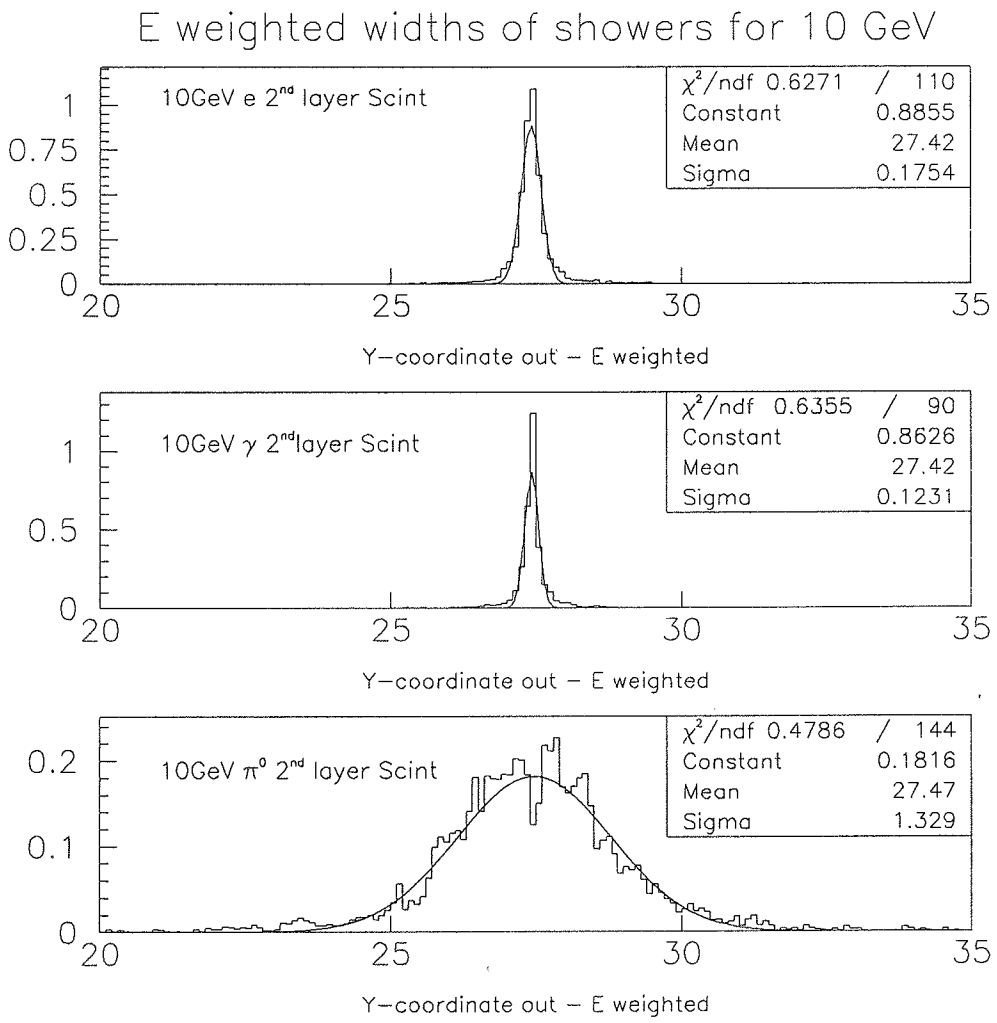

Figure 30: Energy weighted lateral hit distributions in cm of 10 GeV e, γ, and π^0 at $\eta = 2.35$

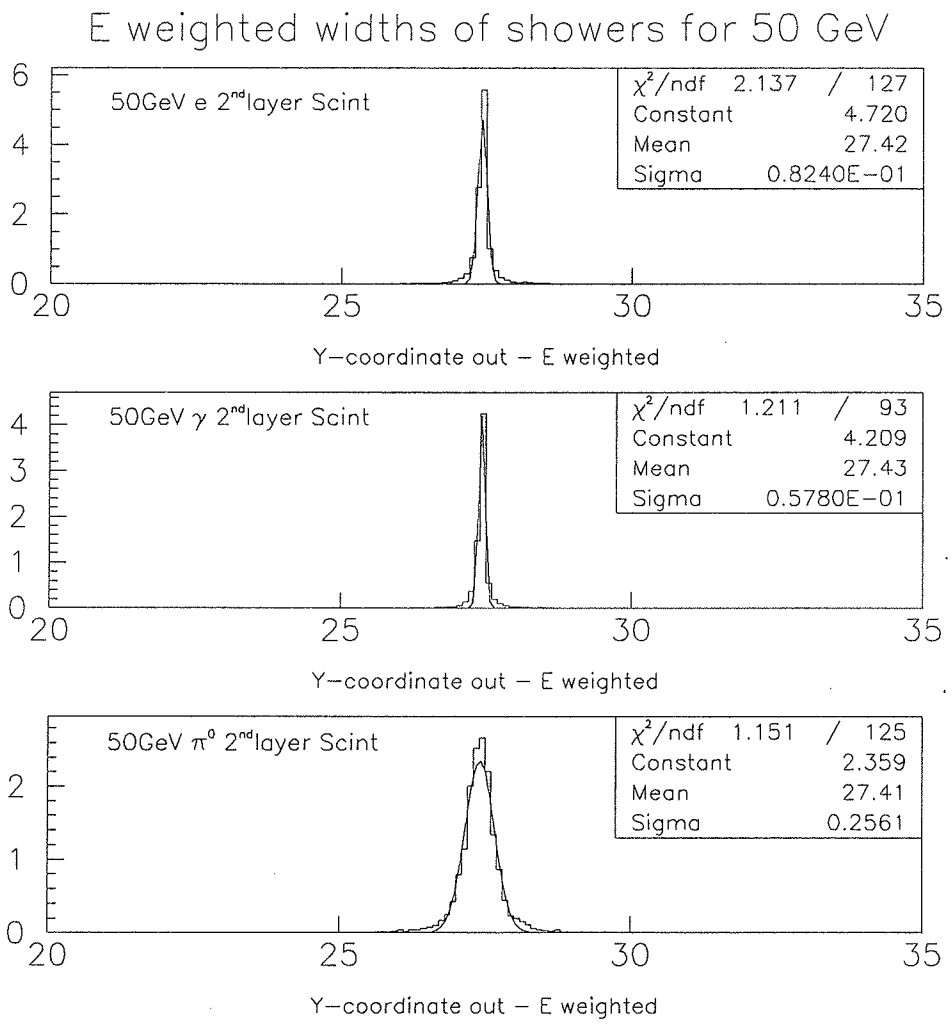

Figure 31: Energy weighted lateral hit distributions of 50 GeV e, γ, and π^0 at $\eta = 2.35$

Energy (GeV)	Δr (mm)		
	e	γ	π^0
10	3.5	2.4	26
50	1.64	1.12	5.1

Table 8: Shower sizes of e, γ, and π^0 for 90% energy containment.

parameterizations. Table 8 summarizes the size of showers in the second layer of the scintillator for various particles with two different energies. The size of showers in the table are for 90% energy containment.

4.2.7 EM energy resolution

To understand the effect of the FPD on the ECEM energy resolution, we performed a Monte Carlo study using 50 GeV electrons at $\eta = 2.35$ with and without the FPD in place. These electrons were then reconstructed with the DØ official reconstruction program, DØRECO V11.19. The FPD energy was not added to the total energy of the electrons (due to technical ZEBRA difficulties – this will be implemented soon). We also did not reoptimize the sampling weights for ECEM layers. Therefore, all distributions show uncorrected shower energies. Figure 32 shows the energy deposition in four layers of ECEM with and without the FPD. The solid histograms indicate the energy deposition with the FPD in place and the dotted line represents otherwise. The energy distribution for each layer shows differences with and without the FPD in place as expected. One can observe an early shower initiation. The electron shower maximum shifts slightly to the second layer of ECEM.

Figure 33 shows the total reconstructed energy distribution with and without the FPD. The electron energy resolution is $19\%/\sqrt{E}$ without the FPD and $30\%/\sqrt{E}$ with the FPD. The latter resolution reflects the worst case scenario where the FPD is in place but is not functioning. The EM energy resolution is worsened by 50% compared to the case without the FPD. One can also observe that the mean value of

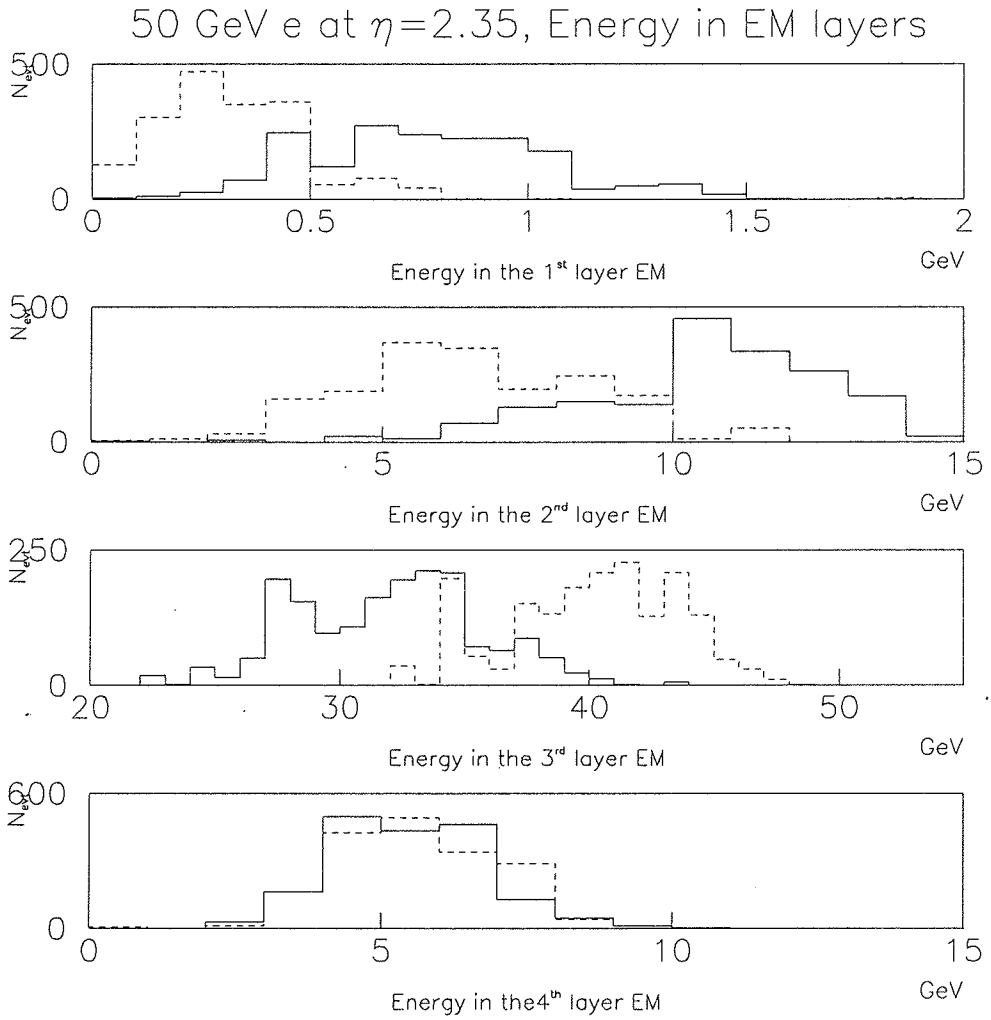

Figure 32: Energy per layer for 50 GeV electrons. Solid histograms show the energy with the FPD in place. Dotted histograms represent the energy without the FPD.

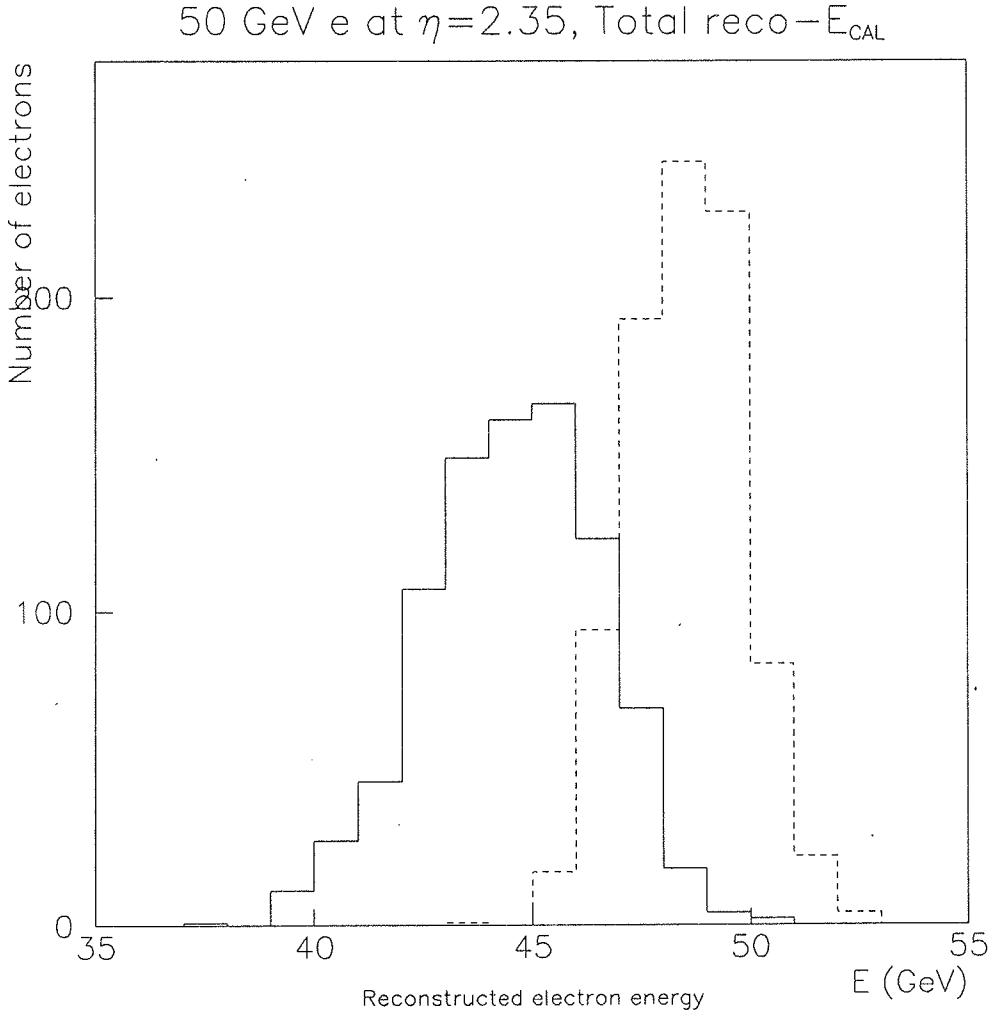

Figure 33: Total reconstructed energy of 50 GeV electrons using ECEM with default sampling weights. Dotted line represent the energy without the FPD. The solid histogram illustrates the energy with the FPD in place without adding the energy deposited in the FPD.

the distribution with the FPD is somewhat lower than that without the FPD. This is because the energy deposited in the FPD is not added and the sampling weights are not properly adjusted for the addition of material in front of the EC. However, the response and energy resolution will get better when the FPD energy is added with properly optimized sampling weights in each layer of ECEM.

4.3 Conclusion

We propose a forward preshower detector to help with electron and photon identification, measurement and triggering in the forward region. A baseline design is presented. Studies show some of the capabilities of the proposed detector. Further studies are underway. A budget and schedule is appended to the end of this document.

5 INTEGRATION ISSUES

5.1 $ICD^{+} + EMICD = ICD^{++}$

The primary design requirements for the intermediate region and the forward region are sufficiently different that building a single integrated detector may not be optimal. Some of the arguments for building separate detectors are:

- The segmentation in the intermediate region follows the pseudo-projective tower geometry of the liquid argon calorimeter – $\eta = 0.1, \phi = 0.1$; whereas much smaller segmentation is required for the FPS.
- Dynamic range required is much larger (by 10^2) for the ICD/EMICD.

Our first goal is to design a new ICD^{++} to withstand the central magnetic field in the DØ upgrade. We plan to preserve as much of the existing ICD in the new design as possible to reduce cost. Scintillators and fibers can work in magnetic fields and therefore remain our preferred choice as the sampling media. However, we will

pursue R&D to increase the light output, since every alternative to the present design requires some deterioration in photon detection efficiency.

Based on our experience in designing the current ICD, there are two possibilities to explore in order to increase the light yield. First, we can use larger diameter PMMA fibers with fluoropolymer cladding. Previous tests done by us for the test beam project have shown that these wavelength shifting fibers may increase light yield as much as 50%. In addition, we can increase the depth of the fiber grooves in the scintillator. Tests done for the current ICD design showed that deeper grooves can proportionately increase light yields.

5.2 Space Integration

On the south side, there is a service chimney containing the cryogenics for the magnet. It leaves the bulkhead via a 6" OD pipe (in the z direction) at 06:00. This nozzle is about 2 inches long, and it connects with the special "obround" 3"x7" chimney at right angles to it (ie which goes in an x-y direction), and which is aligned 14.6 degress below the horizontal as it goes outward in the CC-EC gap. (Note: it does not go on a purely radial path!) The ICD^{++} will have a "gap" to aviod interference with this chimney.

On the north side, extending downward at 6 o'clock, there is a 3" diameter by 3" in z bulkhead connector containing instrumentation cables.

Currently, the magnet bulkhead extends to 53.740 inches in z. Its inner and outer diameters are 20.977 and 27.866 inches, respectively. A 1/4" clearance between the CC and the nominal outer diameter of the preshower detector has been specified. This implies that the absolute location of the radial position of the end bulkhead will be known to that accuracy.

The pseudorapidity range corresponding to the extent of the flat end of the bulkhead is from eta=1.4112 to eta=1.6700 (or theta=0.3722 to theta=0.4784). The radiation length of the magnet as a function of pseudorapidity has been calculated

(see magnet description document).

Much futher work remains to be done on the integration of the various detectors in this region.

6 CONCLUSION

We have proposed substantial improvements to the intermediate and forward calorimeters of the DØ detector. The physics benefits are nummerous. We have done extensive simulation work to show both the feasibility and benefits from these additions. Preliminary designs are presented. We hope that these detectors will become a part of the Run II upgrades to the DØ detector.

7 BUDGET

Category	Sub-Category	Item	Equipment	Operating
Calorimeter				
	ICD	Scintillator	21	
		Fiber	2	
		Misc. supplies	5	
		Tile machining		15
		Assembly	10	5
		Mechanical support	10	5
		New cabling	40	
		New patch boards	10	
		Readout *	102	
			---	--
		ICD Total	200	25
	EMICD	Scintillator	26	
		Fiber	2	
		Lead absorber	3	
		Misc. supplies	5	
		Tile machining		17
		Assembly	10	6
		Mechanical support	10	5
		Cabling	40	
		Patch boards	10	
		ADC-BLS	20	
		Low voltage PS	10	
		Calibration	10	
		Readout *	77	

		---	--
	EMICD Total	223	28
FPD	Scintillator	26	
	Fiber	38	
	Lead absorber	1	
	Misc. supplies	10	
	Tile machining		40
	Assembly	10	15
	VLPC	300	
	Fiber connectors	15	
	Mechanical support	10	5
	Cabling	90	
	Patch boards	10	
	Calibration	50	
		---	--
	FPD Total	560	60
ICD+EMICD+FPD	Prototypes	40	10
	Test Beam	50	10
		--	--
	Test/R&D Total	90	20

All numbers in $k.

8 SCHEDULE

ICD+EMICD Schedule

Item	Start Date	Completion Date
Readout R&D	contd.	Dec 1994
Simulation	contd.	Dec 1994
Prototype (2 phi, all eta)	Jan 1995	Aug 1995
Test & benchmark prototype	Sep 1995	Dec 1995
Engineering/design	Jan 1995	Dec 1995
Procurement	Jan 1996	
Fabrication/assembly	Mar 1996	Dec 1996
QA testing/calibration	Jun 1996	Feb 1997
Shipment to FNAL	Mar 1997	
Installation	Apr 1997	Jun 1997

FPD Schedule

Item	Start Date	Completion Date
Tile R&D	contd.	Dec 1994
Simulation	contd.	Jun 1995
Prototype (mini-wedge)	Jan 1995	Aug 1995
Test & benchmark prototype	Sep 1995	Dec 1995
Engineering/design	Jun 1995	Jun 1996
Procurement	Jun 1996	
Fabrication/assembly	Aug 1996	Mar 1997
QA testing	Dec 1996	Aug 1997
Shipment to FNAL	Sep 1997	

Installation	Oct 1997	Dec 1997
Commissioning	Jan 1998	Jun 1998

ICD+EMICD+FPD TB IV Schedule

Item	Start Date	Completion Date
Test Beam prototype	Jan 1996	Aug 1996
Test Beam run	Nov 1996	Jun 1997

References

[1] DØ Collaboration (S. Abachi *et al.*), "The DØ Detector," Nucl. Inst. &Meth. in Phys. Res. A338, **185** (1994).

[2] M. Tuts, "The DØ Upgrade," DØ Note #1604 (1992).

[3] Q. Zhu, "Measurement of the W Boson Mass in Proton-Antiproton Collisions at $\sqrt{s} = 1.8$ TeV," DØ Note #2160 (1993).

[4] DØ Collaboration (S. Abachi et al.), "Search for the Top Quark in p-pbar Collisions at $\sqrt{s} = 1.8$ TeV," Phys. Rev. Lett. 72, 2138 (1994).

[5] The ALEPH Collaboration, "Heavy Flavour Production and Decay with Prompt Leptons in the ALEPH Detector," CERN-PPE/94-017 (1994).

[6] M. Paterno, "A Search for Squarks and Gluinos in p-pbar Collisions at $\sqrt{s} = 1.8$ TeV with the D0 Detector," Ph.D. Thesis, State University of New York at Stony Brook, May 1994.

[7] CDF Collaboration (F. Abe et al.), "Limits on the Production of Massive Stable Charged Particles," Phys. Rev. D46, 1889 (1992).

[8] DØ Collaboration (S. Abachi *et al.*), Phys. Rev. Lett. 72, 2332 (1994).

For further details of analysis see B. May, Ph.D. thesis, University of Arizona (1994) (unpublished).

[9] H. Piekarz & J. Wightman, "Analysis of Events with Large Total Transverse Energy," DØ Note #2315 (1994).

[10] P. Aurenche *et al* in "Physics at Fermilab in the 1990's", Breckenridge, Colorado, August 15-24 (1989) *pp* 212 (eds. D. Green & H. Lubatti).

[11] K. Maeshima for the CDF collaboration, in "Proceedings of the 9th topical workshop on proton-antiproton collider physics," Ed. K. Kondo and S. Kim, Universal Academy Press, Inc., Tokyo, Japan, 109 (1993).

[12] R. Partridge, "The LevelØ Trigger," DØ Note #1295 (1991).

[13] Jaehoon Yu, "Determination of the Strong Coupling Constant (α_s) and a Test of Pertubative QCD Usingt W + jets Processes in the DØ Detector", SUNY-Stony Brook dissertation (1993).

[14] References on the CDF End Plug Calorimeter include: G. Apollinari, et al., "CDF End Plug Calorimeter Upgrade Project", University of Rochester preprint UR-1329.

P. de Barbaro, et al., "CDF Plug Upgrade Hadron Calorimeter Design", CDF Note CDF/DOC/PLUG_UPGR/CDFR/2545, 06 May, 1994.

[15] References on the SDC Calorimeter tile/fiber include: The SDC Collaboration, "The Solenoidal Detector Collaboration Technical Design Report", SDC-92-201, Apr. 1, 1992.

V. Hagopian, et al., "Single Tile-Fiber Unit of SDC Calorimeter", SDC-92-020, July 17, 1992.

K. Hara, et al., "Number of Photoelectrons of Scintillating Tile/Fiber Assemblies", SDC-93-442, Feb. 5, 1993.

[16] J. Kotcher for the DØ Collaboration, "Inclusive Jet and Direct Photon Production at the DØ Experiment," in the "Proceedings of the 9th topical workshop on proton-antiproton collider physics," Ed. K. Kondo and S. Kim, Universal Academy Press, Inc., Tokyo, Japan, (1993).

[17] Yi-Cheng Liu, private communication. .

[18] A. Taketani for the DØ Collaboration, in "Proceedings of the 9th topical workshop on proton-antiproton collider physics," Ed. K. Kondo and S. Kim, Universal Academy Press, Inc., Tokyo, Japan, (1993).

[19] DØ Collaboration (S. Abachi et al.), "Measurement of the $WW\gamma$ gauge boson coupling at the Tevatron Collider," in preparation.

[20] These numbers were calculated by Tony Spadafora.

[21] K. De &T.L. Geld, "A First Look at Comparative Hadronic Energy Resolution in the ICD Region from Test Beam Data," DØ Note #1272 (1991).

[22] R. Stephens, "Energy Corrections for the CC/EC Transition Region," DØ Note #1165 (1991).

[23] L. Oesch, K. De & H.A. Neal, "The Design, Construction and Testing of the DØ ICD Laser Calibration System," DØ Note #1273, (1992).

[24] K. De et al., "Proposed Design for a Photomultiplier Tube Testing Facility," DØ Note #952, (1990).

[25] K. De, "Tests of the DØ Calorimeter Response in 2-150 GeV Beams," Proceedings of the XXVI International Conference on High Energy Physics, Dallas, TX, August 6–12 (1992).

[26] S. Abachi et al., "Beam tests of the DØ uranium liquid argon end calorimeters," Nucl. Inst. &Meth. in Phys. Res. A53 (1993).

[27] K. De, editor, "Proceedings of the ICD Workshop of March 27, 1990," DØ Note #952 (1990).

[28] H. Aihara, et al., Nucl. Instrum. Methods **A325**, 393(1993).